https://doi.org/10.1016/j.engstruct.2021.113317

Structural testing and numerical modelling of T-joints between cold-formed S690 circular hollow sections under brace in-plane bending

Yi-Fei Hu[1,2] , Kwok-Fai Chung[1,2*], Huiyong Ban[3] and David A. Nethercot[4]

[1]*Department of Civil and Environmental Engineering, The Hong Kong Polytechnic University, Hong Kong SAR, China.*

[2] *Chinese National Engineering Research Centre for Steel Construction (Hong Kong Branch) The Hong Kong Polytechnic University, Hong Kong SAR, China.*

[3] *Department of Civil Engineering, Tsinghua University, China.*

[4] *Department of Civil and Environmental Engineering, Imperial College London, U.K.*

** Corresponding author: kwok-fai.chung@polyu.edu.hk*

ABSTRACT

This paper presents a comprehensive investigation into the structural behaviour of T-joints between high strength S690 cold-formed circular hollow sections (CFCHS) under brace in-plane bending, and deformation characteristics of these T-joints under both monotonic and cyclic actions are examined experimentally and simulated numerically. These T-joints between S690 CFCHS were found to deform with a high level of resistances and ductility under both monotonic and cyclic actions.

Through an integrated numerical modelling approach developed by the authors, advanced three-dimensional finite element models of CFCHS with solid elements were established. With a proper definition of weld collars at the brace/chord junctions of the T-joints between S690 CFCHS with different diameters and thicknesses, these models were readily adopted to perform a heat transfer analysis, a thermomechanical analysis and a structural analysis sequentially with compatible element types and meshes. Hence, the effects of the welding-induced residual stresses at the welded brace/chord junctions onto the structural behaviour of these T-joints were readily assessed. Consequently, these advanced models are demonstrated to be able to predict rationally deformation characteristics of these T-joints between S690 CFCHS under monotonic and cyclic actions of brace in-plane bending with a high degree of structural accuracy.

Keywords:

T-joints between high strength CHS; cold-formed circular hollow sections; monotonic and cyclic actions; brace in-plane bending; resistance and ductility.

NOTATIONS

d_0	Outer diameter of the chord
d_1	Outer diameter of the brace
n_c	Number of cycle completed before failure
q	Heat input energy
t_0	Wall thickness of the chord
t_1	Wall thickness of the brace
f_y	Yield strength of steel
f_{y0}	Yield strength of the chord
f_u	Ultimate strength of steel
E	Young's modulus
E_{el}	Reference elastic dissipated energy
E_i	Dissipated energy at each cycle
E_i^+ and E_i^-	Energy dissipated in the tension and the compression half-cycles
E_{acc}	Accumulative energy dissipation
I	Welding current
L	Span between two pinned supports of a T-joint between CFCHS
L_0	Length of the chord
L_1	Length of the brace
$M_{j,FE}$	Predicted moment resistance of a T-joint from numerical analyses
$M_{j,FE+}$	Maximum positive moment from numerical analyses
$M_{j,FE-}$	Maximum negative moment from numerical analyses
$M_{j,R}$	Measured moment resistance of the chord of a T-joint predicted to CIDECT or EN 1993-1-8 with a reduction factor for high strength steels
$M_{j,Rd}$	Design moment resistance of a T-joint
$M_{j,Rt}$	Measured moment resistance of a T-joint

$M_{j,Rt+}$	Maximum positive moment
$M_{j,Rt-}$	Maximum negative moment
N_x	Measured lateral load applied to the T-joint
$N_{x,el}$	Reference elastic lateral load at first yield
$N_{x,FE}$	Predicted lateral load resistance of the T-joint from numerical analyses
$N_{x,Rt}$	Measured lateral load resistance of the T-joint
$N_{x,Rt+}$	Maximum positive lateral load
$N_{x,Rt-}$	Maximum negative lateral load
S_i	Initial tangent slope
α	Chord length parameter
β	Brace to chord diameter ratio
2γ	Chord diameter to chord thickness ratio
τ	Ratio of brace wall thickness to chord wall thickness
Δ	Displacement measured with displacement transducers
$\Delta_{j,x}$	Lateral displacement of a T-joint
$\Delta_{j,x,f}$	Lateral displacement of a T-joint at failure
$\Delta_{j,x,FE}$	Predicted lateral displacement of a T-joint at failure
$\Delta_{j,x,el}$	Displacement of a T-joint under reference elastic load $N_{x,el}$
Δ_u	Displacement measured at failure
σ_e	Engineering stress
σ_t	True stress
ε_e	Engineering strain
ε_t	True strain
ε_u	Elongation at tensile strength
ε_f	Elongation at fracture
θ_b	Rotation of a T-joint

$\theta_{b,m}$	Maximum interstorey drift
η_a	Energy dissipation ratio

1. Effective use of high strength cold-formed hollow sections

As steel-making technologies have been significantly developed in the past twenty years, high strength steel cold-formed structural hollow sections, such as S460, S550 and S690 circular and rectangular hollow sections, are produced in many parts of the world, and they are readily available in a wide range of shapes and dimensions nowadays. The advantages of high strength S690 cold-formed circular hollow sections (CFCHS) are widely recognized among structural engineers. These S690 CFCHS are highly efficient structural members because of their effective structural forms with large rigidities against torsion and buckling. Owing to their large strength to self-weight ratios, these S690 CFCHS are often adopted in heavily loaded as well as long spanning structures. In addition to a direct saving in steel materials, there are significant savings in materials and labour costs for welding of these S690 CFCHS because of reduced numbers of welding passes.

In general, welding of these S690 steels may induce significant reductions to the mechanical properties of welded sections and joints, in particular, in the vicinity of their heat affected zones (HAZ). However, by a proper control on the welding processes, it has been demonstrated that there is no reduction in the section resistances of these S690 welded sections and joints [1, 2]. It is important to limit the amount of heat input energy onto these steels during welding so that even though microstructural change is initiated, there is only limited time for phase change, recrystallization and grain growth in the HAZ of these steels to take place. Hence, there is no deterioration in their mechanical properties. It should be noted that the threshold values of the heat input energy during welding depend on many metallurgical and physical factors, such as chemical compositions and heat treatments of the steels, as well as plate thicknesses, joints details and various welding procedures and parameters.

1.1 Structural behaviour of T-joints through laboratory testing

As there were many research projects which examined structural behaviour of joints between structural hollow sections in the past thirty years, only those directly relevant to the present investigation, i.e. T-joints between cold-formed structural hollow sections under monotonic and cyclic actions were reported.

Wang and Chen [3] examined the hysteretic behaviour of T-joints between S355 CHS under cyclic actions. For those T-joints under cyclic brace axial compression, they were found to fail in i) weld fracture under tension, and ii) chord plastification under compression. For those T-joints under cyclic brace in-plane bending, they were found to fail in punching shear and chord plastification together with weld fracture. Moreover, an experimental investigation on a total of twelve T-joints between high strength CHS were conducted by Kim et al. [4], and all of these T-joints were tested under cyclic brace in-plane bending. Curved coupons were extracted from these sections, and their yield strengths were found to be 464 and 584 N/mm^2. It was shown that all of these T-joints failed in chord plastification under large brace in-plane moments, and their ductility compared very well with those T-joints between S355 CHS.

Both Havula et al. [5] and Hu et al. [6] carried out experimental investigations into the structural behaviour of T-joints between S420 to S700 structural hollow sections under monotonic brace in-plane bending. It was shown that these T-joints failed in chord plastification, and strain hardening was well developed at failure. Although fracture at the HAZ was often observed in these T-joints after excessive plastic deformations, the rotational capacities of these T-joints were found to be well above the commonly adopted 3% deformation limit [7, 8, 9]. Hence, the structural behavio0075r of these T-joints was shown to be adequate in terms of both resistance and ductility at large deformations.

1.2 Structural behaviour of T-joints through numerical simulation

With a continual development on advanced finite element modelling on steel structures over the past thirty years, there were a large number of modelling technique on the structural

behaviour of joints between structural hollow sections available in the literature. Many numerical studies simulated different deformation characteristics of T-joints between structural hollow sections with different sizes and shapes under various actions. Owing to complex geometry of the brace/chord junctions in these T-joints, it was often very difficult to use either hole-drilling method or sectioning method to measure welding-induced residual stresses of these joints. Hence, the effects of welding-induced residual stresses in welded sections and joints were assessed through advanced finite element modelling in the recent years.

In order to simulate the weld geometry for accurate predictions on joint resistances, the numerical models were usually constructed with solid elements. Lee et al. [10] conducted a detailed numerical study on X-joints between cold-formed CHS to examine their compression behaviour; the nominal yield strength of these CHS was 650 N/mm^2. It should be noted that while the weld geometry was carefully incorporated into the proposed models, the mechanical properties of the weldment were assumed to be the same as those of the steels for simplicity.

Lan et al. [11] conducted a systematic numerical simulation into the structural behaviour of X-joints between high strength circular hollow sections of steel grades ranging from S460 to S1100. It should be noted that the effects of welding onto the mechanical properties of these joints were incorporated through applying a set of reduction factors to the HAZ of the welded joints. It should be noted that a trial and error process was conducted to establish the values of these reduction factors in various parts of the HAZ after achieving good comparisons between the measured and the predicted load-deformation curves of these X-joints.

Garifullin et al. [12, 13] developed a numerical model to determine welding-induced residual stresses in T-joints between S420 hot-finished rectangular hollow sections through a sequentially coupled thermomechanical analysis with the finite element software Abaqus [14]. It should be noted that no direct heat transfer analysis was performed, and instead, element temperatures were inputted into the proposed model. Hence, three-dimensional stress analyses using solid elements C3D8R were performed to obtain thermomechanical as well as structural

responses of T-joints. The model was considered to be a simplistic one as the heat input energy in the T-joints was not quantified directly.

1.3 Previous research conducted by the authors

In order to promote effective use of high strength S690 steels in construction, a comprehensive research programme was conducted by the authors since 2011, and a number of experimental investigations [15, 16, 17, 18, 19, 20] on mechanical properties of the S690 steels and structural behaviour of their welded sections were conducted:

- Compression tests on 12 stocky and 16 slender columns of S690 welded H-sections
- Bending tests on 18 partially restrained S690 welded I-sections
- Compression tests on 8 stocky and 12 slender columns of S690 CFCHS

In order to improve predictability of the structural behaviour of these S690 welded sections, an integrated numerical modelling approach [21] was proposed to simulate two major fabrication processes of these sections, namely, i) transverse bending, and ii) longitudinal welding, in particular for CFCHS, as shown in Fig. 1, with the following advanced models:

a) Transverse bending was simulated in a two dimensional model with plane strain elements as *a three-roller bending process* for CFCHS, followed by an elastic spring back. A comprehensive comparison on residual stresses of these CFCHS between measured values and predicted as well as theoretical values was conducted and reported [21].

b) Longitudinal welding was simulated in a three dimensional model as i) *a heat transfer process*, and ii) *a thermomechanical process* in a sequentially coupled analysis to determine the residual stresses with solid elements. Material and thermal properties of the steels at elevated temperatures and various parameters on heat input energy during welding were fully incorporated into the model for both the heat transfer and the thermomechanical processes. A thorough comparative study on these welding-induced

residual stresses of these CFCHS between measured values and predicted values was reported in detail [21].

It should be noted that these advanced models had been successfully calibrated against

- measured surface residual strains after transverse bending and elastic spring back; and
- measured transient temperature distributions during longitudinal welding, and surface residual strains after longitudinal welding.

Hence, the residual stresses in both the transverse and the longitudinal directions of these CFCHS due to the two major fabrication processes were readily incorporated into the advanced models for subsequent structural analyses.

In general, there is an obvious deficiency in experimental data on the deformation characteristic of T-joints between high strength S690 CFCHS, especially for those T-joints under monotonic and cyclic actions. The effects of welding-induced residual stresses on the structural behaviour of these T-joints remain uncertain. Consequently, there is a clear need to develop advanced models to simulate the structural behaviour of these T-joints between S690 CFCHS with welded brace/chord junctions.

As the proposed integrated approach has been demonstrated [22, 23, 24, 25, 26] to be effective to simulate residual stresses due to both transverse bending and longitudinal welding within the S690 CFCHS, this approach is expanded in the present investigation to simulate the welding-induced residual stresses at the brace/chord junctions of these T-joints between S690 CFCHS. Then, the models are employed to examine the structural behaviour of these T-joints between S690 CFCHS under both monotonic and cyclic actions of brace in-plane bending.

1.4 Objectives and scope of work

This paper presents a comprehensive investigation into the structural behaviour of T-joints between high strength S690 cold-formed circular hollow sections (CFCHS) under brace in-

plane bending, and deformation characteristics of these T-joints under both monotonic and cyclic actions were examined experimentally and simulated numerically. Deformation characteristics of these T-joints under both monotonic and cyclic actions are captured in carefully executed experiments, and analysed rationally [6].

Through the integrated numerical modelling approach proposed by the authors [21], advanced three-dimensional finite element models of CFCHS with solid elements were established. With a proper definition of weld collars at the brace/chord junctions of the T-joints between S690 CFCHS with different diameters and thicknesses, these models were readily adopted to perform a heat transfer analysis, a thermomechanical analysis and a structural analysis sequentially with compatible element types and meshes. Hence, the effects of the welding-induced residual stresses at the welded brace/chord junctions onto the structural behaviour of these T-joints were readily assessed. The predicted load displacement curves of those T-joints under cyclic actions were examined, and their hysteretic behaviour were quantified with various parameters.

The research project comprises of the following:

a) Experimental investigation

   Two tests on the T-joints between high strength S690 CFCHS, namely, Tests M-T1 and M-T2, were carried out under monotonic brace in-plane bending, as shown in Fig. 2a), to determine their basic deformation characteristics. Another test on the T-joint between normal strength S355 CFCHS, namely, Test M-T0, with nominally identical dimensions to those joints in Tests M-T1 and M-T2, was also carried out under a similar loading condition to provide reference data for subsequent comparison.

   Moreover, another four tests on the T-joints, namely, Tests C-T3 and C-T4, and Tests C-T5 and C-T6, were carried out under cyclic brace in-plane bending, as shown in Fig. 2b). All the measured test data were then analysed and presented as representative cyclic

deformation characteristics of these T-joints. These deformation characteristics were then quantified through the use of various parameters to describe their hysteretic behaviour.

b) Numerical investigation

In order to examine the structural behaviour of these T-joints between S690 CFCHS with the presence of welding-induced residual stresses in the welded brace/chord junctions, advanced finite element models with solid elements were established. It should be noted that the welding process of the brace/chord junctions of these T-joints was simulated directly through sequentially coupled thermomechanical analyses using the finite element software Abaqus. Hence, in each of these models, a heat transfer analysis was performed to evaluate transient temperature distributions in the junction during welding, and then, a thermomechanical analysis was also performed to evaluate "locked-in" stresses and strains in the junction after welding.

In order to simulate the deformation characteristics of those T-joints under monotonic actions of brace in-plane bending, a structural analysis on the advanced models was conducted. Comparison between the predicted and the measured deformation characteristics of the joints was made to calibrate the proposed models. These models were then extended to simulate deformation characteristics of the other joints under cyclic actions of brace in-plane bending. It should be noted that their hysteretic behaviour were simulated with the standard kinematic models together with a set of suitably selected parameters after a careful calibration against test data.

Key areas of interest are:

- structural behaviour of these T-joints between S690 CFCHS under i) monotonic brace in-plane bending, and ii) cyclic brace in-plane bending;
- advanced finite element models of these T-joints with a proper definition of weld collars along the welded brace/chord junctions for simulation of welding

- an accurate prediction on deformation characteristics of the T-joints under both monotonic and cyclic actions, both of brace in-plane bending; and
- various parameters to quantify the hysteretic behaviour of these T-joints, such as i) number of cycles completed before failure, ii) deterioration under cyclic actions, and iii) energy dissipation up to failure.

It should be noted that after calibration against the test results of the T-joints with S690 CFCHS under both monotonic and cyclic actions, the proposed models will be employed to perform a comprehensive parametric study to predict the structural behaviour of these T-joints over a wide range of diameters and thicknesses. Comparison of the numerical resistances with the design values according to modern structural design codes will also be made. The findings of these work will be reported in a separate paper.

2. Experimental Investigation

2.1 Test programme

A total of six T-joints between S690 CFCHS and a T-joint between S355 CFCHS were tested in the present investigation, and these T-joints were grouped into two different test series, as shown in Fig. 2, according to the following test conditions:

- Series M: T-joints under monotonic actions
  - Joints M-T1 and M-T2 with Joint M-T0 as a reference
- Series C: T-joints under cyclic actions
  - Joints C-T3 and C-T4, and Joints C-T5 and C-T6.

The test programme of these T-joints is summarized in Table 1 together with nominal dimensions of both the braces and the chords and their geometric parameters. It should be noted that all of these T-joints are nominally identical in their dimensions. The measured dimensions of these T-joints are summarized in Table 2.

2.2 Fabrication process of T-joints

The overall configuration of these T-joints between S690 CFCHS is shown in Fig. 3, and they were fabricated in a well-equipped fabrication plant through the following processes:

i) after being cut to sizes, the steel plates were press-braked with a circular punch along their longitudinal edges, and then bent transversely using a three-roller machine to achieve their circular forms;

ii) the longitudinal free edges of these circular sections were welded up using a gas metal arc welding (GMAW) with a welding electrode ER110S-G according to AWS A5.28 [27] to form a CFCHS; and

iii) after a careful positioning of both the brace and the chord, the brace/chord junction was also welded up using a GMAW with a combination of fillet and partial penetration welds.

It should be noted that all the welding was performed by a qualified welder, and the chemical compositions of these welding electrodes are presented in Table 3 while their mechanical properties are listed in Table 4. Typical measured dimensions of the weld collars at specific locations of the welded junctions of the T-joints are presented in Fig. 4.

It should be noted that the heat input energy during welding of all the CFCHS and the welded junctions were carefully controlled to range from 1.2 to 1.5 kJ/mm. Hence, there is no significant reduction in the mechanical properties of these S690 sections and joints according to previous experiences of the authors [1, 2]. For details of the fabrication of these CFCHS, refer to Hu et al.[21].

2.3 Material properties

Standard tensile tests on curved coupons extracted from both the S355 and the S690 CFCHS were carried out according to BS EN ISO-6892-1 [28], and the basic mechanical properties of these CFCHS are presented in Table 5.

2.4 Test set-up and loading procedures

2.4.1 Series M: T-joints under monotonic actions

Fig. 2a) illustrates the test set-up for T-joints under monotonic actions of brace in-plane bending, and these joints were tested with a 1,500 kN hydraulic jack. In each test, the T-joint was installed carefully with the help of laser levels so that the steel pins at both ends of the chord were well positioned onto the supports, and the brace was properly aligned with the line of action of the hydraulic jack. It should be noted that the joint was simply supported so that lateral movement was allowed to take place in one support only through slotted holes in the base plate.

The following loading procedure was adopted in each test:

a) In order to eliminate initial bedding in the test set-up, a pre-loading process was performed for at least three times. During each pre-loading process, a load up to 30% of the estimated joint resistance was applied slowly to the joint, and then, released in 3 to 5 steps so that the joint was allowed to return to its unloaded position.
b) After a successful elimination of any initial bedding, the load was steadily applied to the joint at a rate of 30 to 50 kN per minute up to 80% of the estimated joint resistance. Then, the load was applied through a manual control on displacement at 1 to 2 mm per minute until occurrence of either a sudden failure or a definite unloading. The load resistance of the joint, $N_{x,Rt}$ was taken to be the maximum applied load.
c) The test was terminated after the applied load dropped below 80% of the value of $N_{x,Rt}$.

Fig. 2c) illustrates typical instrumentation of the test. It should be noted that the applied load was measured with a load cell, a total of eight displacement transducers were used to measure the overall displacements of the T-joint, and three strain gauges were used to measure axial strains of the brace. All these data were captured and recorded at close time intervals throughout the tests.

2.4.2 Series C: T-joints under cyclic actions

Fig. 2b) illustrates the test set-up for T-joints under cyclic actions of brace in-plane bending, and these joints were tested with a 1,000 kN actuator under a hydraulic servo control testing system. In each test, a cyclic load N_x was applied to the joint through the brace end, and the magnitude of the applied load varied according to:

a) Loading Protocol SAC

   Cyclic actions in the form of a drift angle θ_b was imposed to the joints of both Joints C-T3 and C-T4 according to SAC [29] as well as ANSI/AISC 341-16 [30], which was illustrated in Fig. 5a).

b) Loading Protocol to ECCS

   According to ECCS [31], cyclic tests on Joints C-T5 and C-T6 were conducted through imposing alternate positive and negative displacements Δ_j^+ and Δ_j^- respectively, as illustrated in Fig. 5b).

It should be noted that Loading Protocol SAC is widely adopted in structural tests of structural members under seismic actions while Loading Protocol ECCS is commonly adopted for experimental investigations into cyclic behaviour of structural components and members. Moreover, the loads were applied through a displacement control at a rate of 2 to 3 mm/min. Both the test set-up and the instrumentation of these T-joints are identical to those for Joints M-T0, M-T1 and M-T2 described in the previous section.

In both Series M and C, initial out-of-straightness of all the T-joints was measured before testing, as shown in Fig 6. As these T-joints were fabricated in a qualified steelwork fabricator, the workmanship of fabrication, in particular, pre-welding alignment and distortion control, was guaranteed. Moreover, in each test, measurements were made to the T-joint after it was installed onto the supports, and adjusted carefully to achieve proper alignments. As both the

final values of v_1 and v_2 after alignment were often found to be smaller than 0.5 to 1.0 mm, the effects of initial out-of-straightness of the T-joints onto their behaviour was considered to be very small.

2.5 Test results

All the tests in both Series M and C were conducted successfully, and they were terminated when there was a sudden drop in the applied loads immediately after failure in the joints. Details of the test results are presented in the following sections.

2.5.1 Failure modes

For those T-joints in Series M under monotonic actions, Fig. 7 illustrates the deformed shapes of Joints M-T0, M-T1 and M-T2 just before failure of the joints. A close examination at the joints after the tests revealed a fracture in the HAZ of the brace in the vicinity of the welded brace/chord junction of each of Joints M-T1 and M-T2. However, there was no such a fracture found in Joint M-T0 though apparent local deformations in its brace/chord junction were evident.

For those T-joints in Series C under cyclic actions, Fig. 8 illustrates the deformed shapes of Joints C-T3 and C-T4, and also of Joints C-T5 and C-T6 just before failure of the joints. A close examination at the joints after the tests revealed a fracture in the HAZ of the braces in the vicinity of the welded brace/chord junctions of all these joints. Owing to the presence of large co-existing bending moments and shear forces, apparent deformations were found in the welded junctions of all these joints.

2.5.2 Applied load versus lateral displacement curves

Fig. 9 plots the applied load versus lateral displacement (N_x - $\Delta_{j,x}$) curves of the T-joints in Series M while Fig. 10 plots those of the T-joints in Series C. According to the instrumentation shown in Fig. 2c), the lateral displacement of the joint, $\Delta_{j,x}$, is readily determined as

$$\Delta_{j,x} = \Delta_1 - \frac{\Delta_4 - \Delta_6}{2} \quad (1)$$

where

Δ_1 , Δ_4 and Δ_6 are the measurements of Transducers L01, L04 and L06.

It should be noted that for those T-joints in Series M under monotonic actions, the (N_x - $\Delta_{j,x}$) curve of Joint M-T0 was found to demonstrate a ductile deformation even after the resistance of the joint was fully mobilized at a large displacement up to 135.0 mm. According to the (N_x - $\Delta_{j,x}$) curves of both Joints M-T1 and M-T2, their deformation characteristics was also considered to be fairly ductile. However, a sudden fracture in the HAZ of the braces occurred after full mobilization of their joint resistances, and the lateral displacements $\Delta_{j,x}$ of Joints M-T1 and M-T2 reached 84.7 and 87.7 mm, respectively.

It is important to determine two reference quantities, namely, the reference elastic load of the joint at first yield, $N_{x,el}$ and the corresponding displacement $\Delta_{j,x,el}$, from the load-displacement curves; both of them are used to define commencement of non-linear behaviour of the T-joint. According to Section 3.1 of ECCS, the value of $N_{x,el}$ is defined graphically as the intersection between the initial tangent slope S_i and the tangent with a slope of S_i / 10, both of the applied load versus lateral displacement curves, as illustrated in Fig. 9. The values of $N_{x,el}$ and $\Delta_{j,x,el}$ for the joints are found to be 120.3 kN and 30.1 mm, and they are adopted for subsequent analyses in Section 2.6 Energy dissipation characteristics.

For those T-joints in Series C under cyclic actions, the hysteretic (N_x - $\Delta_{j,x}$) curves of Joints C-T3 and C-T4 under Loading Protocol SAC are plotted in Fig. 10a) while those of Joints C-T5 and C-T6 under Loading Protocol ECCS are plotted in Fig. 10b). The numbers of cycles completed before failure, n_c , are also presented in the graphs for direct reference. It is evident that the hysteretic curves of all these four joints demonstrate highly favourable cyclic deformation characteristics without significant softening in stiffness nor significant

deterioration in resistances throughout the cyclic tests. Their maximum lateral displacements $\Delta_{j,x}$ were found to vary from 47.7 to 66.1 mm for both Loading Protocols.

2.5.3 Joint resistances

The measured in-plane moment resistance, $M_{j,Rt}$, of each T-joint is defined as follows:

$$M_{j,Rt} = r \cdot N_{x,Rt}$$

where $N_{x,Rt}$ is the measured lateral load at failure, and

r is the distance from the line of action of the applied load to the top surface of the chord.

For those T-joints in Series M under monotonic actions, Table 6 summarizes the test results of Series M, and a comparison between the measured and the design moment resistances according to EN 1993-1-8 [9] is also provided. The moment resistance of Joint T-M0 was found to be 58.1 kNm while the average moment resistance of Joints T-M1 and T-M2 was found to be 101.5 kNm. It was shown that

a) A comparison on the yield strengths of the braces in Joints M-T0, M-T1 and M-T2 revealed that despite there was an increase of about 2.01 in the yield strengths of the S690 steels when compared with that of the S355 steels, the corresponding increase in the joint resistances was merely 1.75. It should be noted that there was a change in failure modes, i.e. from yielding in a S355 brace to a HAZ fracture in both S690 braces.
b) The moment resistances of both Joints M-T1 and M-T2 have been fully mobilized before the occurrence of a HAZ fracture in the braces, and hence, the sudden fracture did not cause a significant reduction in the joint resistances though there was a moderate reduction in ductility.

c) The model factors $\frac{M_{j,Rt}}{M_{j,Rd}}$ of the three T-joints are found to range from 1.26 to 1.28, and hence, the design rule given in EN 1993-1-8 is shown to be able to predict the design resistances of these T-joints conservatively.

For those T-joints in Series C under cyclic actions, Table 7 summarizes the test results of Series C. Both the positive moment resistances $M_{j,\,Rt+}$ and the negative moment resistances $M_{j,\,Rt-}$ of these joints were found to be very close to the measured value from the monotonic tests reported above, i.e. 101.5 kNm. The numbers of cycles completed before failure, n_c , were also summarized together with the corresponding displacements for comparison. It should be noted that

a) For Joints C-T3 and C-T4, the averaged values of $M_{j,Rt+}$ and $M_{j,Rt-}$ were shown to be 95.6 and 96.7 kNm respectively, there were only 4.7 to 5.8% reductions in the joint resistances up to failure of the joints.
b) For Joints C-T5 and C-T6, the averaged values of $M_{j,Rt+}$ and $M_{j,Rt-}$were shown to be 101.6 and 99.6 kNm respectively, and reductions in the joint resistances were found to be smaller than 1.8% up to failure of the joints. The skeleton curves of the load-displacement curves of Joint C-T4, and Joint C-T6 were plotted in different graphs in Fig. 11, each with the measured load-displacement curve of Joint M-T2 for a direct comparison. It should be noted that these skeleton curves are found to be very similar to one another throughout the entire deformation ranges though there is a small deterioration in the deformation characteristics, when compared with those of the Joints under cyclic actions to both Loading Protocols.

2.6 Energy dissipation characteristics

The energy dissipation characteristics of the T-joints under cyclic brace in-plane bending are evaluated by the energy dissipation ratio, η_a [3,32]. In each T-joint, the dissipated energy per cycle E_i of cycle i is defined as the area enclosed by the load-displacement curve, as shown in Fig. 12, and it is calculated as follows:

$$E_i = E_i^+ + E_i^- = A_{PQR} + A_{RSP} \quad (2)$$

where

E_i^+ and E_i^- are the energy dissipated in the tension and the compression half-cycles respectively;

A_{PQR} and A_{RSP} are the areas enclosed by Curves *PQR* and *RSP*, respectively, in Fig.12.

Hence, the energy dissipation ratio, η_a , is calculated as follows:

$$\eta_a = \sum_{i=1}^{n_c} \frac{E_i^+ + E_i^-}{E_{el}} \quad (3)$$

$$E_{el} = \frac{N_{x,el}\,\Delta_{j,x,el}}{2} \quad \text{from a monotonic test} \quad (4)$$

It should be noted that the values of $N_{x,el}$ and $\Delta_{j,x,el}$ were determined to be 120.3 kN and 30.1 mm according to the load-displacement curves of Tests M-T1 and M-T2, as shown in Fig. 9. Hence, the value of E_{el} was found to be 1.80 kNm.

The dissipated energy per cycle E_i , the accumulative energy dissipation E_{acc} and the calculated energy dissipation ratios η_a of Joints C-T3 to C-T6 are summarized in Table 8. It should be noted that the dissipated energy per cycle in the first 18 cycles is found to be very small, and hence, they are not considered in the calculation.

As shown in Table 8, the accumulative energy dissipation E_{acc} of both Joints C-T3 and C-T4 are significantly larger than those of Joints C-T5 and C-T6 because of the differences in the Loading Protocols, and hence, the numbers of cycles complete before failure, n_c . The values

of E_{acc} are found to be significantly larger than the value of E_{el} , and hence, the corresponding values of the energy dissipation ratios η_a range from 1.97 to 30.15. It should be noted that the energy dissipation ratios η_a of both Joints C-T3 and C-T4 are larger than the threshold value of 4.0 stipulated in the energy dissipation requirements given in the Recommended Practice of the American Petroleum Institute [33]. Therefore, these two T-joints are considered to have adequate energy dissipation capacities for application in seismic resistant structures under Loading Protocol SAC. It should be noted that based on the experimental results of these T-joints, Loading Protocol SAC is preferred in the present investigation as it is able to examine the structural behaviour of the T-joints over a wide range of deformations under practical loadings, without the need of having a monotonic test in advance. Both the hysteretic behaviour and the energy dissipation characteristics of the T-joints are readily captured under Loading Protocol SAC.

3 Numerical investigation

In order to examine the structural behaviour of these T-joints between S690 CFCHS with the presence of welding-induced residual stresses in the welded brace/chord junctions, an integrated numerical modelling approach developed by the authors [21] using the finite element software Abaqus [14] is adopted. An overall view of the proposed integrated approach with sequentially coupled thermomechanical and structural analyses are employed for determination of the deformation characteristics of a typical T-joint, as shown in Fig. 13. It should be noted that:

a) the welding process is simulated in a heat transfer analysis using *heat transfer elements DC3D8* in which a heat source is adopted to impose a heating / cooling cycle to the brace/chord junction to determine the transient temperature distributions;
b) the welding process is then simulated in a thermomechanical analysis using *stress elements C3D8R* in which the transient temperature distributions are adopted to determine the

"locked-in" stresses and strains of the brace/chord junction during contraction after welding; and

c) the bending process is then simulated in a structural analysis using *the same stress elements C3D8R* in which both the monotonic and the cyclic actions of brace in-plane bending are adopted to determine the deformation characteristics of the T-joints.

The proposed finite element model of a typical T-joint between S690 CFCHS is illustrated in Fig. 14, and the detailed configuration of the mesh of the T-joint, in particular, the welded brace/chord junction and the weld collar, is shown. Various parameters for physical, thermal and mechanical properties of the steel materials at elevated temperatures given in EN1993-1-2 [34] are incorporated into the models. It should be noted that the proposed integrated approach with sequentially coupled thermomechanical analyses have been calibrated thoroughly against measured surface temperatures and measured surface residual stresses of S690 CFCHS [21]. Specific details for modelling these T-joints are provided in the following sections.

3.1 Material properties

In the proposed models, the stress-strain curves of both the chord and the brace obtained from curved coupon tests are converted to true stress-strain curves, as shown in Fig. 15a), through the following equations:

$$\varepsilon_t = \ln(1 + \varepsilon_e) \quad \text{5a)}$$

$$\sigma_t = \sigma(1 + \sigma_e) \quad \text{5b)}$$

where

ε_e and ε_t are the engineering and the true strains of the steel materials, and

σ_e and σ_t are the engineering and the true stresses of the steel materials.

An elastic-perfectly plastic model is assigned to be the stress-strain curves of the welds. The initial elastic modulus of the weld is taken also to be 210 kN/mm^2 according to EN 1993-1-1 [35]. Hence, the true stress-strain curve of the weld is shown in Fig. 15b). It should be noted that the Poisson's ratio of both the steels and the weld is taken as 0.3, and both the isotropic hardening rule and the von Mises yield criterion are adopted.

No fracture mechanism is considered in the present investigation, and hence, no initiation of cracks nor their propagation are incorporated in the proposed models of the T-joints. For those T-joints under cyclic in-plane bending, hardening of the steels is considered by adopting a widely accepted approach of a combined isotropic and kinematic hardening models reported in the literature [36, 37, 38].

3.2 Boundary conditions and mesh sizes

The boundary conditions of the proposed models for both heat transfer and thermomechanical analyses are shown in Fig. 16a). For structural analyses, the boundary conditions of the proposed models are shown in Fig. 16b), and three reference points have been set up to couple all the nodes at both the chord ends and the brace end. It should be noted that all the models are loaded with a lateral displacement applied onto Reference Point R_o through the static general method given in Abaqus/Standard [14].

In general, a total of three layers of solid elements are provided across the thickness of these CFCHS in order to capture local bending behaviour adequately. Regular meshes are adopted in the present numerical investigation to achieve high numerical accuracy and convergence, in particular, in non-linear heat transfer as well as in thermomechanical analyses. It should be noted that by adopting the optimal aspect ratios of the solid element C3D8R, the mesh size at the weld collars is assigned to be 5.0 (r) x 5.0 (s) x 2.0 (t) mm after several trial runs. It should be noted that the total number of solid elements in each model is about 140,000, and the average execution time per run is found to range from 12 to 16 hours using a high power computer. In general, the effects of initial geometrical imperfections onto the structural behavior of these T-

joints under in-plane bending are considered to be small as these T-joints fail in material yielding or fracture rather than member buckling.

3.3 Generation of appropriate meshes for welded brace/chord junctions

Fig. 17 illustrates the weld collar along the brace/chord junction of the T-joint. There are two welding passes, and each welding pass is modelled as a series of four welding steps, each along a quarter of the circular collar.

It should be noted that it is always a major task in establishing both the shapes and the sizes of hundreds of non-regular solid elements accurately to form the weld collar of the proposed models according to the measured dimensions given in Fig. 4. This has been achieved with a rigorous implementation of an advanced three-dimensional spatial modelling algorithm to generate coordinates of all the intersection points of two circular hollow sections with different diameters and plate thicknesses. The problem is further complicated when multi-pass welding is adopted, and these elements are required to be grouped into two or more collars according to various welding parameters. All the elements of each welding step, i.e. a quarter of the welding collar, are added simultaneously as one group of elements, and the modelling technique of "element birth and death" is adopted only in the sequentially coupled thermomechanical analysis. Hence, all the material properties of these elements are "switched on" during heat transfer analysis. For further details of the modelling technique, refer to Reference [40].

3.4 Predicted transient temperature distributions from heat transfer analyses

In the proposed models, the welding process for the brace/chord junction is simulated through a total of two welding passes, and there are four welding steps along the CFCHS in each pass, as shown in Fig. 17. In each step, a ramp model is employed to simulate the heat source moving

over a quarter of the circular collar [39, 40]. The moving action is achieved by adjusting the value of the heat input energy, q, kJ/mm against time, as illustrated in Fig. 18:

$$q = \eta U \times I / v \quad (6)$$

where

η is the welding efficiency,

U & I are the voltage (V), and the current (A) of the welding arc; and

v is the welding speed (mm/s).

It should be noted that the voltage and the current of the welding arc together with the welding speed were measured during welding of all these T-joints. As the value of η was taken conservatively as 0.85 for GMAW method, the value of q was found to range from 1.2 to 1.5 kJ/mm. Hence, a line heat energy of 1.35 kJ/mm was adopted for numerical analyses. For details of the heat transfer analyses, refer to Hu et al. [21].

The transient temperature distribution obtained from the heat transfer analyses during welding is shown in Fig. 19a) immediately after completion of the first welding pass, and in Fig. 19b) immediately after completion of the second welding pass. It should be noted that the grey region represents a molten electrode with a temperature above 1500 °C.

3.5 Predicted residual stress distributions from thermomechanical analyses

Based on the predicted transient temperature distributions of the welded brace/chord junctions of these T-joints obtained from the heat transfer analyses, a thermomechanical analysis according to temperature changes, i.e. heating up during welding, and then, cooling down after welding, of the steels is performed. Hence, the "locked-in" stresses and strains, or the residual stresses and strains, are readily determined according to differential thermal contraction of both the brace and the chord. For details of the thermomechanical analyses, refer to Hu et al. [21].

The residual stress distributions at the welded brace/chord junction of a typical T-joint after welding is shown in Fig. 20. Variations of surface residual stresses at both the crown and the

saddle points of the welded brace/chord junction are also illustrated, and it is clearly shown that the residual stresses reach their maximum values right at the weld collars, as expected. It should be noted that these stresses are highly localized, and do not spread beyond the weld collar significantly.

3.6 Calibration of the proposed models under monotonic actions

It is important to calibrate the proposed models against test data in order to ensure a high accuracy in the predicted deformation characteristics of these T-joints. Fig. 21a) illustrates a comparison on the deformed T-joints of both Model M-T2 and Joint M-T2 while a comparison of the measured and the predicted applied load versus lateral displacement ($N_x - \Delta_{j,x}$) curves of Joints M-T0, M-T1 and M-T2 is shown in Fig. 21b). It is clearly demonstrated that the predicted curves of the proposed models follow closely the measured values of the joints. In order to assess the deformation characteristic of the T-joint, a deformation limit is proposed in order to prevent excessive local deformations in the brace/chord junctions. And their moment resistances are determined by adopting the failure criterion recommended in Annex C of EN 1993-1-5 [41], i.e. when the maximum principal strain achieves 5%. In general, this deformation limit is considered to be sufficiently large to replicate the situation of fracture. And this also provides a reasonable margin against the elongation limit of the S690 steels at 10%. Hence, the predicted moment resistances of these T-joints under monotonic actions are summarized in Table 6 for a direct comparison with those measured values. It is shown that the ratios of the measured to the predicted joint moment resistances, $M_{j,Rt} / M_{j,FE}$, range from 0.99 to 1.02 with an average value at 1.003.

Hence, the proposed models are demonstrated to be able to predict the deformation characteristics of these T-joints with a high accuracy, in particular, the initial stiffness, the load resistances and the corresponding lateral displacements.

3.6.1 A comparative study on heat input energy

A comparative study on the effects of the heat input energy q adopted during welding of the brace/chord junctions onto the structural behaviour of Joint M-T1 is carried out. Three models are adopted in which the values of the heat input energy q were assigned to be 0.0, 1.35 and 2.0 kJ/mm. It should be noted that the value of 2.0 kJ/mm is often considered to be a practical maximum for GMAW, and it is readily achieved with a single welding pass. With these heat input energy adopted during the numerical simulation of welding, the corresponding residual stresses at the brace/chord junctions are illustrated in Fig. 22. It is shown that:

- For the model with q = 2.0 kJ/mm with a single welding pass, the residual stresses induced at both the inner and the outer surfaces of the collar are fairly high. As the surface areas in the saddle regions are increased locally, their residual stresses are found to be smaller than those at the crown regions.
- For the model with q = 1.35 kJ/mm with two welding passes, the residual stresses induced at the inner surface of the collar in Pass 1 are found to be significantly smaller than those of the outer surface in Pass 2 which are found to range from 700 to 800 N/mm^2, i.e. the largest among all shown in Fig. 22.

Nonlinear structural analyses on these models with full incorporation of these residual stresses are performed, and various plots on different deformation characteristics of the T-joints with a maximum principal strain at 5% are illustrated in Fig. 23. It should be noted that

- The plots on principal strains of the models with q = 0.0, 1.35 and 2.0 kJ/mm are found to be very similar to another, and large and highly localized tensile strains are developed in the vicinity of the weld collar where initiation of fracture takes place in the test.
- All the plots on von Mises stresses of the models with q = 0.0, 1.35 and 2.0 kJ/mm are also found to be very similar.

- The applied load versus lateral displacement ($N_x - \Delta_{j,x}$) curves of the models with q = 0.0, 1.35 and 2.0 kJ/mm and Joints M-T1 and M-T2 show that the predicted load-displacement curves follow closely the measured curves throughout the entire deformation ranges of the joints.

Table 9 summarizes the predicted moment resistances obtained from the proposed models with q = 0.0, 1.35 and 2.0 kJ/mm, together with the measured values of Joints M-T1 and M-T2. The ratios of the measured to the predicted resistances, $M_{j,Rt} / M_{j,FE}$ are shown to range from 0.99 to 1.02. Hence, the effects of residual stresses at the welded brace/chord junctions onto the structural behaviour of these T-joints are found to be very small.

3.7 Cyclic deformation characteristic of the proposed models under cyclic actions

After a successful calibration of the proposed models under monotonic actions, the proposed models with q = 1.35 kJ/mm are extended to predict the structural behaviour of the T-joints under cyclic actions according to the measured values of q reported in Section 3.4. It should be noted that the constitutive model of the S690 steels with a combined isotropic and kinematic hardening rules with two numbers of back stresses [36, 37, 38] are adopted to model strain hardening in the steels under cyclic actions in which the yield surface of the steels shifts in stress space as straining in one direction reduces the yield strength in the opposite direction. Based on typical results of tensile tests, the constitutive model is able to account for i) isotropic effects in hardening, including the Bauschinger effect and anisotropy, and ii) progressive hardening effects with a non-linear kinematic hardening behaviour.

Fig. 24 illustrates a typical deformed model of one of the T-joints and the corresponding observed deformations under cyclic brace in-plane bending, and it is apparent that the predicted deformations of the T-joint compare well with the observed deformations. In addition, comprehensive comparisons between the predicted and the observed deformed shapes of the

T-joints in Series M and C, together with various gross deformations in the vicinity of the brace/chord junctions, are also presented in Fig. 7 and 8, respectively.

Both the measured and the predicted applied load versus lateral displacement ($N_x - \Delta_{j,x}$) curves of Joints C-T3 and C-T4, and Joints C-T5 and C-T6 under cyclic actions are plotted in Fig. 25. The proposed models are shown to be able to predict the hysteretic curves of these T-joints under both Loading Protocols with a high accuracy.

The values of both the predicted maximum positive moments, M_{max}^{+}, and the predicted maximum negative moments, M_{max}^{-} of the proposed models are also presented in Table 7 for a direct comparison with those measured values. It should be noted that the differences between the predicted and the measured values of the positive moment resistances, M_{max}^{+} , of these T-joints are found to be smaller than 3%, and the average values of the moment resistance ratios $M_{j,Rt}^{+}$ / $M_{j,FE}^{+}$ are shown to range from 0.97 to 1.02. Similarly, the differences between the predicted and the measured values of the negative moment resistances, M_{max}^{-} , of these T-joints are also found to be smaller than 3%, and the average values of the moment resistance ratios $M_{j,Rt}^{-}$ / $M_{j,FE}^{-}$ is shown to range from 0.97 to 1.00.

Moreover, the maximum measured values of the lateral displacement $\Delta_{j,x}$ and the corresponding values of N_x in each cycle of both the predicted and the measured hysteretic curves of all the T-joints are plotted in Fig. 26. It is shown that the predicted loads N_x are very close to those of the measured values. Table 10 summarizes those predicted and measured loads N_x after the first eighteen cycles, together with the discrepancy ratios. It is shown that the average values of the discrepancy ratios are found to range from 1.46 to 2.30 % for Models C-T3 and C-T4, and 1.43 to 3.15 % for Models C-T5 and C-T6.

Both the predicted dissipated energy per cycle, E_i , and the accumulative energy dissipation, E_{acc}, of the T-joints are also presented in Table 8 for a direct comparison with the measured

ones, and it is shown that for Model C-T3, the measured and the predicted values of E_{acc} are found to be 54.27 and 56.14 kNm over a total of 36 cycles. For Model C-T4, the measured and the predicted values of E_{acc} are found to be 27.29 and 21.42 kNm over a total of 34 cycles. Similarly, for Model C-T5, the measured and the predicted values of E_{acc} are found to be 15.89 and 15.33 kNm over a total of 5 cycles. For Model C-T6, the measured and the predicted values of E_{acc} are found to be 3.55 and 2.61 kNm over a total of 4 cycles.

Hence, the proposed models are demonstrated to be able to predict the deformation characteristics of these T-joints between S690 CFCHS under cyclic brace in-plane bending with a high level of accuracy.

4. Conclusions

This paper presents a comprehensive investigation into the structural behaviour of T-joints between high strength S690 cold-formed circular hollow sections (CFCHS) under brace in-plane bending, and deformation characteristics of these T-joints under both monotonic and cyclic actions were examined experimentally and simulated numerically. Deformation characteristics of these T-joints under both monotonic and cyclic actions were captured in carefully executed experiments, and analysed rationally [6].

Through an integrated numerical modelling approach developed by the authors [21], advanced three-dimensional finite element models of CFCHS with solid elements were established. With a proper definition of weld collars at the brace/chord junctions of the T-joints between S690 CFCHS with different diameters and thicknesses, these models were readily adopted to perform a heat transfer analysis, a thermomechanical analysis and a structural analysis sequentially with compatible element types and meshes. Hence, the effects of the welding-induced residual stresses at the welded brace/chord junctions onto the structural behaviour of these T-joints were readily assessed. The predicted load displacement curves of those T-joints under cyclic actions were examined, and their hysteretic behaviour were quantified with various parameters.

After careful data analysis and interpretation on both the experimental and the numerical results, the following conclusions are drawn:

a) The T-joints between S690 CFCHS under monotonic brace in-plane bending, i.e. Joints M-T1 and M-T2, are found to fail with a fracture in the heat-affected zones of the braces in the vicinity of the welded brace/chord junctions. The maximum lateral displacements of these T-joints are found to exceed the lateral displacement corresponding to 5% principal strains in the joints. Interestingly, the T-joints between S690 CFCHS under cyclic brace in-plane bending, i.e. Joints C-T3 and C-T4, and Joints C-T5 and C-T6, are also found to have a similar failure. Hence, the sudden fracture does not pose any adverse effect on these joints as their resistances have been fully mobilized well before the occurrence of the fracture.

b) Through an integrated numerical modelling approach, advanced three-dimensional finite element models of the T-joints between S690 CFCHS with solid elements are established to simulate welding through sequentially coupled thermomechanical analyses. With a proper definition of weld collars at the brace/chord junctions of the T-joints between S690 CFCHS with different diameters and thicknesses, residual stresses under a specific value of the heat input energy are predicted. The corresponding structural behaviour of the T-joints under both monotonic and cyclic actions of brace in-plane bending are then readily predicted. It is also demonstrated that the proposed models are able to predict the hysteretic deformation characteristics of these T-joints with a high level of structural accuracy, in particular, the hysteretic applied load versus lateral displacement ($N_x - \Delta_{j,x}$) curves and the corresponding energy dissipation. However, no prediction on the fracture behaviour of these joints is incorporated due to its complexity.

c) Welding-induced residual stresses along the welded brace/chord junctions are found to have limited effects onto the structural behaviour of these T-joints under brace in-plane bending, in particular, both the moment resistances and the ductility. Consequently, the effects of welding onto the structural behaviour of these T-joints are shown to be

significantly less pronounced than generally anticipated, provided that the welding processes and parameters have been properly controlled.

It should be noted that the proposed models will be employed to perform a comprehensive parametric study to predict the structural behaviour of these T-joints over a wide range of diameters and thicknesses. Comparison of the numerical resistances with the design values according to modern structural design codes will also be made. The findings of these work will be reported in a separate paper.

Acknowledgments

The research work leading to publication of this paper was supported by the Research Grants Council of the University Grants Committee of the Government of Hong Kong SAR (General Research Funds - Project Nos. PolyU 152194/15E, 1526871/16E, 152231/17E and 152157/18). Moreover, the work is supported by the Chinese National Engineering Research Centre for Steel Construction (Hong Kong Branch) at the Hong Kong Polytechnic University which is funded by the Innovation and Technology Fund of the Government of Hong Kong SAR and the Research Committee of the Hong Kong Polytechnic University (Account Nos. 1-BBY3 and 1-BBVY). The research studentship provided by the Research Committee of the Hong Kong Polytechnic University to the first author (Project No. RTZX) is also gratefully acknowledged.

REFERENCES

[1] Ho, H. C., Chung, K. F., Huang, M. X., Nethercot, D. A., Liu, X., Jin, H., & Tian, Z. H. (2020). Mechanical properties of high strength S690 steel welded sections through tensile tests on heat-treated coupons. Journal of Constructional Steel Research, 166, 105922.

[2] Chung, K. F., Ho, H. C., Hu, Y. F., Wang, K., Liu, X., Xiao, M., & Nethercot, D. A. (2020). Experimental evidence on structural adequacy of high strength S690 steel welded joints

with different heat input energy. Engineering Structures, 204, 110051.

[3] Wang, W., & Chen, Y. Y. (2007). Hysteretic behaviour of tubular joints under cyclic loading. Journal of Constructional Steel Research, 63(10), 1384-1395.

[4] Kim, J. W., Kim, S. S., Lee, M. J. and Yang, J. G. (2012). Vierendeel joints in the circular hollow sections of high strength steel subjected to brace moment and chord compressive loadings. International Journal of Steel Structures, 12(4): 579-587.

[5] Havula, J., Garifullin, M., Heinisuo, M., Mela, K., & Pajunen, S. (2018). Moment-rotation behaviour of welded tubular high strength steel T joint. Engineering Structures, 172, 523-537.

[6] Hu, Y. F., Chung, K. F., Jin, H., Ban, H., & Nethercot, D. A. (2021). Structural behaviour of T-joints between high strength S690 steel cold-formed circular hollow sections. Journal of Constructional Steel Research, 182, 106686.

[7] Yura, J. A., Edwards, I. F., & Zettlemoyer, N. (1981). Ultimate capacity of circular tubular joints. Journal of Structural Engineering, 107(10), 1965-1984.

[8] Wardenier, J., Kurobane, Y., Packer, J. A., Van der Vegte, G. J. and Zhao X. L. (2008). Design guide for circular hollow section (CHS) joints under predominantly static loading. CIDECT.

[9] CEN. (2005). BS EN 1993-1-8: Eurocode 3: Design of Steel Structures - Part 1-8: Design of joints. European Committee for Standardization.

[10] Lee, C. H., Kim, S. H., Chung, D. H., Kim, D. K. and Kim, J. W. (2017). Experimental and numerical study of cold-formed high-strength steel CHS X-joints. Journal of Structural Engineering, 143(8), 04017077.

[11] Lan, X., Chan, T. M., & Young, B. (2018). Structural behaviour and design of chord plastification in high strength steel CHS X-joints. Construction and Building Materials, 191, 1252-1267.

[12] Garifullin, M., Launert, B., Heinisuo, M., Pasternak, H., Mela, K., & Pajunen, S. (2018).

Effect of welding residual stresses on local behavior of rectangular hollow section joints. Part 1–Development of numerical model. Bauingenieur: Zeitschrift fuer das gesamte Bauwesen, 93(4), 152-159.

[13] Garifullin, M., Launert, B., Heinisuo, M., Pasternak, H., Mela, K., & Pajunen, S. (2018). Effect of welding residual stresses on local behavior of rectangular hollow section joints. Part 2–Parametric studies. Bauingenieur: Zeitschrift fuer das gesamte Bauwesen, 93(5), 207-213.

[14] Systèmes, D. (2014). Abaqus 6.14 Documentation. Providence, RI: Dassault Systèmes.

[15] Liu, X., Chung, K. F., Ho, H. C., Xiao, M., Hou, Z. X., & Nethercot, D. A. (2018). Mechanical behavior of high strength S690-QT steel welded sections with various heat input energy. Engineering Structures, 175, 245-256.

[16] Ma, T. Y., Liu, X., Hu, Y. F., Chung, K. F., & Li, G. Q. (2018). Structural behaviour of slender columns of high strength S690 steel welded H-sections under compression. Engineering Structures, 157, 75-85.

[17] Ma, T. Y., Hu, Y. F., Liu, X., Li, G. Q., & Chung, K. F. (2017). Experimental investigation into high strength Q690 steel welded H-sections under combined compression and bending. Journal of Constructional Steel Research, 138, 449-462.

[18] Chung, K. F., Ma, T. Y., Li, G. Q., & Yan, X. L. (2021). Behavior and design of high-strength steel columns under combined compression and bending. In Behavior and Design of High-Strength Constructional Steel (pp. 305-355). Woodhead Publishing.

[19] Wang, K., Xiao, M., Chung, K. F., & Nethercot, D. A. (2021). Lateral torsional buckling of partially restrained beams of high strength S690 welded I-sections. Journal of Constructional Steel Research, 184.

[20] Xiao, M., & Chung, K. F. (2021). Structural Behaviour of High Strength S690 Cold-Formed Structural Hollow Sections Under Compression. In EASEC16 (pp. 1559-1568). Springer, Singapore.

[21] Hu, Y. F., Chung, K. F., Ban, H., & Nethercot, D. A. (2020). Investigations into residual stresses in S690 cold-formed circular hollow sections due to transverse bending and longitudinal welding. Engineering Structures, 219, 110911.

[22] Chen, C., Chiew, S. P., Zhao, M. S., Lee, C. K., & Fung, T. C. (2019). Welding effect on tensile strength of grade S690Q steel butt joint. Journal of Constructional Steel Research, 153, 153-168.

[23] Chen, C., Zhang, X., Zhao, M., Lee, C. K., Fung, T. C., & Chiew, S. P. (2017). Effects of welding on the tensile performance of high strength steel T-stub joints. Structures, 9, 70-78.

[24] Lee, C. K., Chiew, S. P., & Jiang, J. (2014). Residual stress of high strength steel box T-joints Part 2: Numerical study. Journal of Constructional Steel Research, 98, 73-87.

[25] Goldak, J., Chakravarti, A., & Bibby, M. (1984). A new finite element model for welding heat sources. Metallurgical Transactions B, 15(2), 299-305.

[26] Liu, X. & Chung, K. F. (2018). Experimental and numerical investigation into temperature histories and residual stress distributions of high strength steel S690 welded H-sections. Engineering Structures, 165, 396-411.

[27] AWS (2005) Specification for Low-Alloy Steel Electrodes and Rods for Gas Shielded Arc Welding. Structural Welding Code – Steel. Miami, United States: American Welding Society.

[28] BS EN ISO 6892-1 (2009). Metallic materials – Tensile testing: Part 1: Method of test at ambient temperature, British Standards Institution.

[29] Clark, P., Frank, K., Krawinkler, H., & Shaw, R., (1997). Protocol for Fabrication, Inspection, Testing, and Documentation of Beam-Column Connection Tests and Other Experimental Specimens, SAC Steel Project Background Document. Report No. SAC/BD-97/02.

[30] AISC. (2016). ANSI/AISC 341-16, Seismic Provisions for Structural Steel

Buildings. Chicago, IL: American Institute of Steel Construction.

[31] ECCS. (1986). Recommended testing procedure for assessing the behaviour of structural steel elements under cyclic loads. Brussels, Belgium: European Convention for Constructional Steelwork.

[32] Soh, C. K., Fung, T. C., Qin, F., & Gho, W. M. (2001). Behavior of completely overlapped tubular joints under cyclic loading. Journal of Structural Engineering, 127(2), 122-128.

[33] API. (2002). American Petroleum Institute, Recommended practice for planning, designing, and constructing fixed offshore platforms. RP2a. Washington (DC).

[34] CEN. (2005). BS EN 1993-1-2: Eurocode 3: Design of Steel Structures - Part 1-2: General rules - Structural fire design. European Committee for Standardization.

[35] CEN. (2005). BS EN 1993-1-1: Eurocode 3: Design of steel structures - Part 1-1: General rules and rules for buildings. European Committee for Standardization.

[36] Halama, R., Sedlák, J., & Šofer, M. (2012). Phenomenological modelling of cyclic plasticity. Numerical Modelling, 1, 329-354.

[37] Wang, H., Yan, Y., Wan, M., & Wu, X. (2012). Experimental investigation and constitutive modeling for the hardening behavior of 5754O aluminum alloy sheet under two-stage loading. International Journal of Solids and Structures, 49(26), 3693-3710.

[38] Ramezansefat, H., & Shahbeyk, S. (2015). The Chaboche hardening rule: A re-evaluation of calibration procedures and a modified rule with an evolving material parameter. Mechanics Research Communications, 69, 150-158.

[39] Brown, S., & Song, H. (1992). Finite element simulation of welding of large structures. Journal of Engineering for Industry, 114(4), 441-451.

[40] Liu, X., Chung, K. F., Huang, M., Wang, G., & Nethercot, D. A. (2019). Thermomechanical parametric studies on residual stresses in S355 and S690 welded H-sections. Journal of Constructional Steel Research, 160, 387-401.

[41] CEN. (2005). EN 1993-1-5: Eurocode 3: Design of Steel Structures - Part 1-5: Plated

structural elements. European Committee for Standardization.

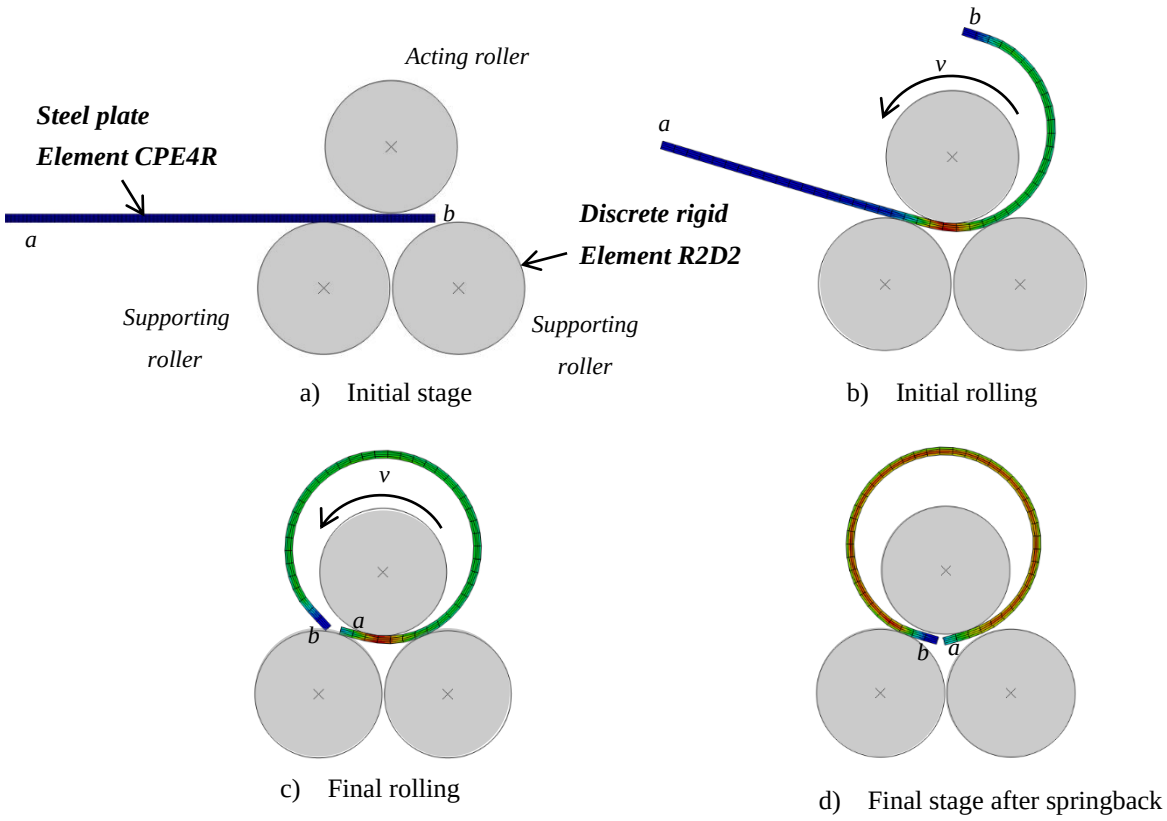

Simulation of transverse bending

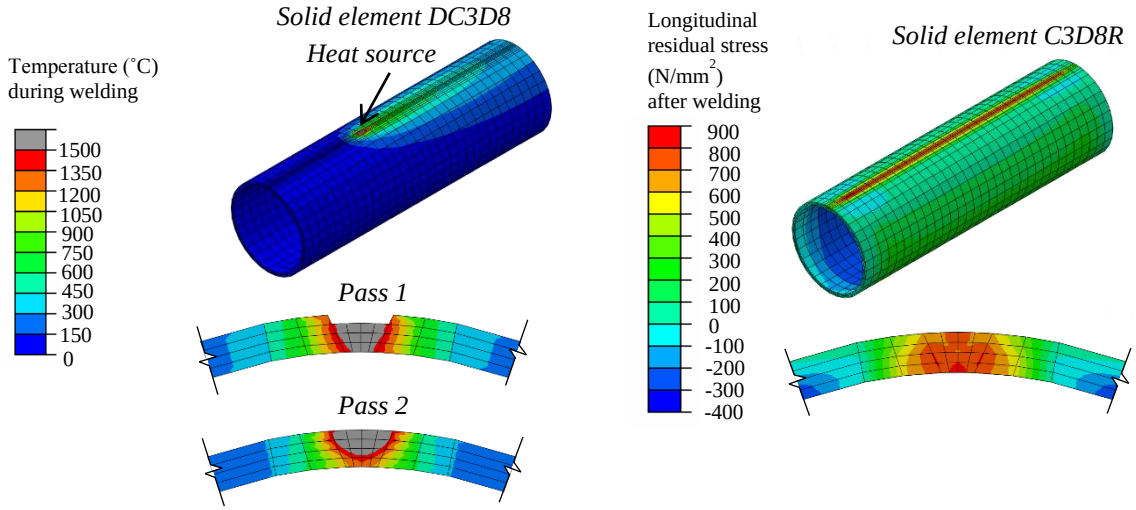

Simulation of longitudinal welding

Figure 1 Numerical modelling of transverse bending and longitudinal welding

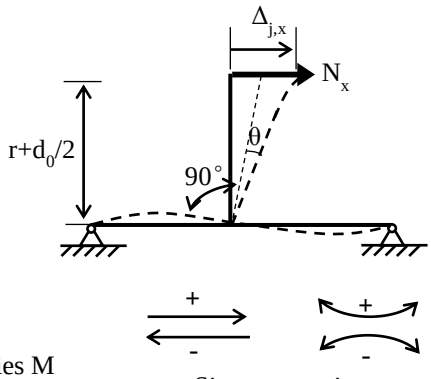

a) Test setup for Series M

Sign convention

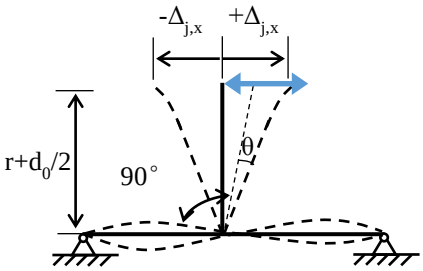

b) Test setup for Series C

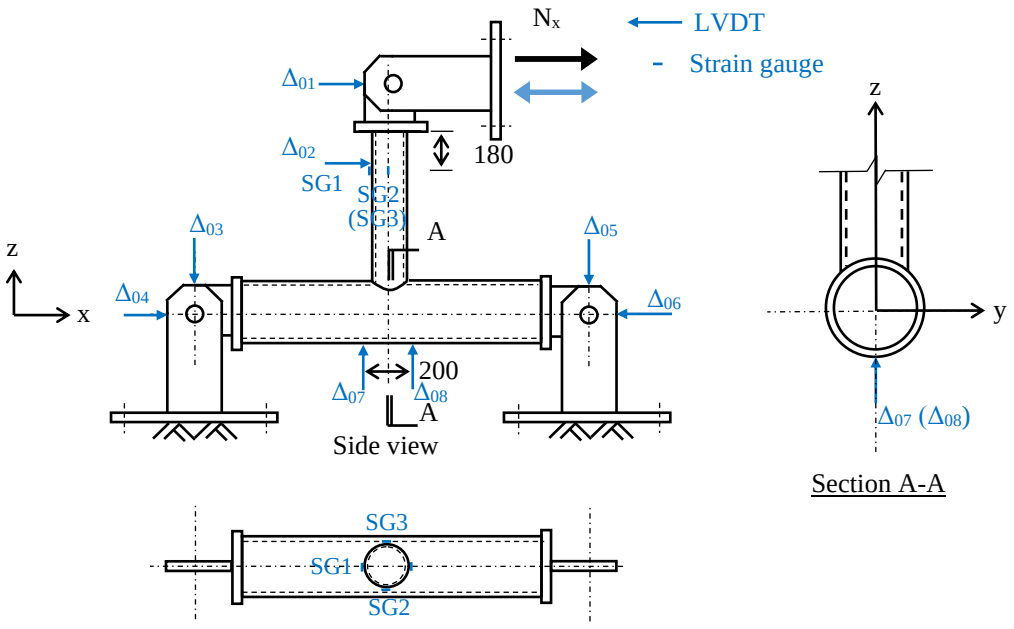

c) Instrumentation for joint tests

Figure 2 Instrumentation for in-plane bending tests on T-joints between CFCHS

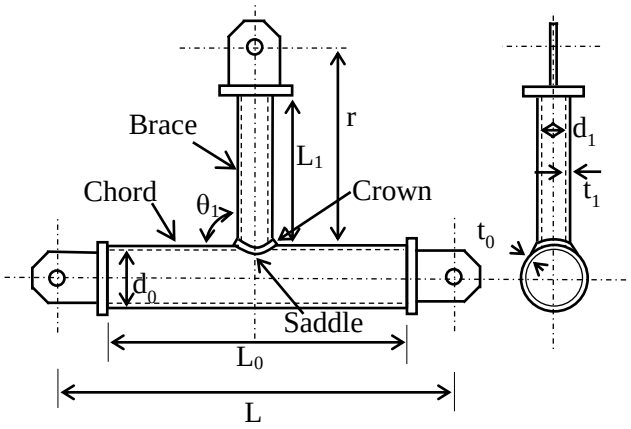

d_0 = 250 mm
t_0 = 10 mm
d_1 = 150 mm
t_1 =6mm
α = $2L_0/d_0$ = 9.6
β = d_1/d_0 = 0.6
2γ = d_0/t_0 = 12.5
τ = t_1/t_0 = 0.6

Figure 3 Overall configuration of a typical T-joint

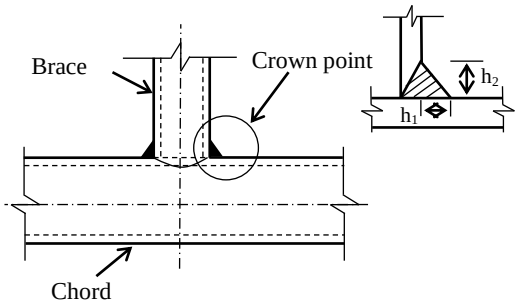

a) Crown point

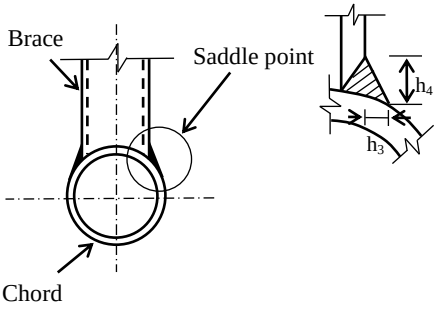

b) Saddle point

Measured weld sizes at crown and saddle points

Joint	h_1 (mm)	h_2 (mm)	h_3 (mm)	h_4 (mm)
M-T0	9.5	11.5	6.9	6.0
M-T1	9.5	10.8	5.0	4.0
M-T2	9.9	12.5	4.5	3.5
C-T3	8.4	11.9	4.8	4.9
C-T4	9.6	9.9	6.4	7.2
C-T5	9.5	12.4	4.3	4.2
C-T6	12.2	11.5	6.1	5.2

Note: line heat energy input = 1.2-1.5 kJ/mm

Figure 4 Welding details of T-joints

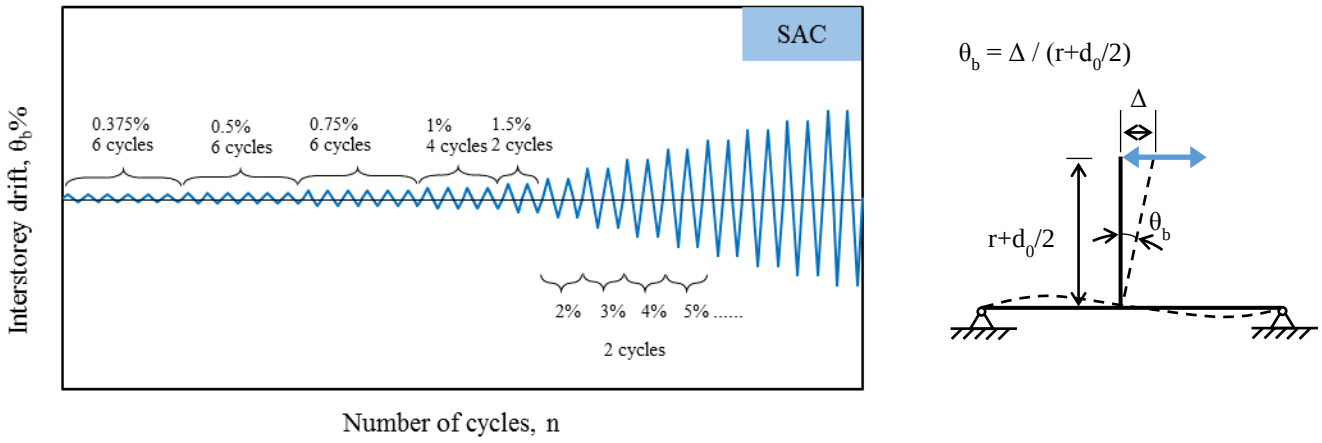

a) Loading Protocol SAC

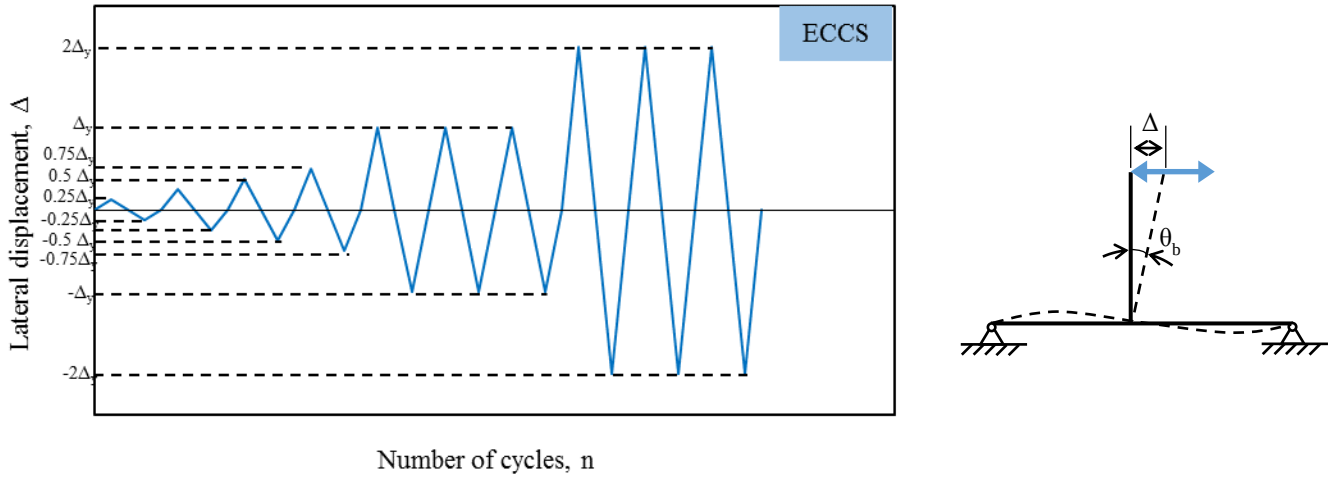

b) Loading Protocol ECCS

Figure 5 Steps defined in loading protocols for cyclic tests

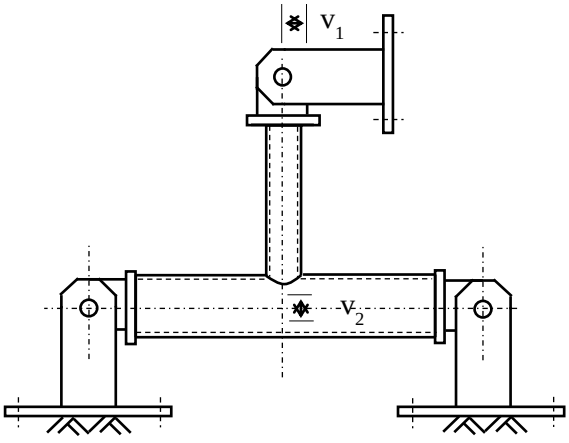

Figure 6 Initial out-of-straightness

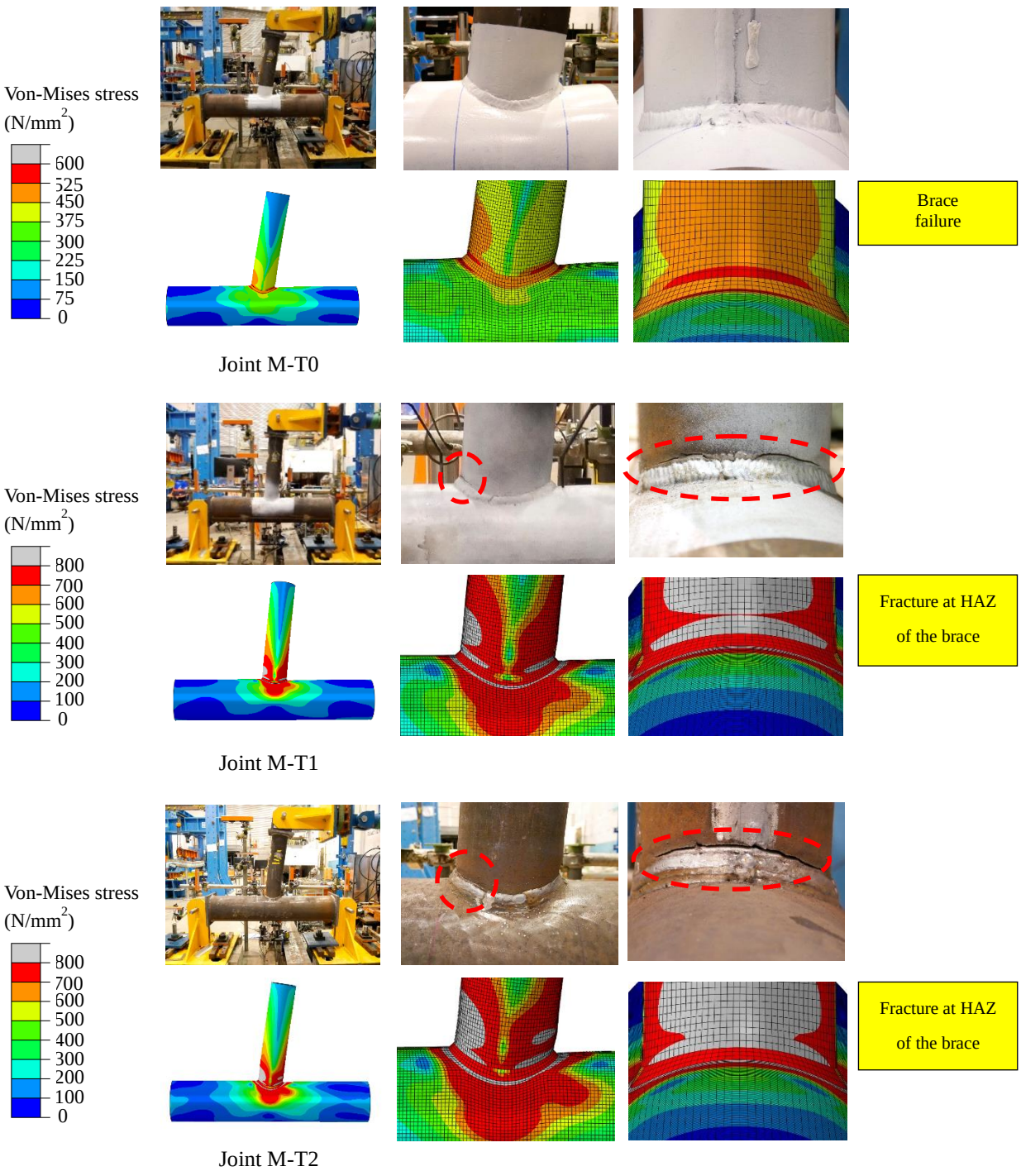

Figure 7 Typical failure modes of T-joints under monotonic actions

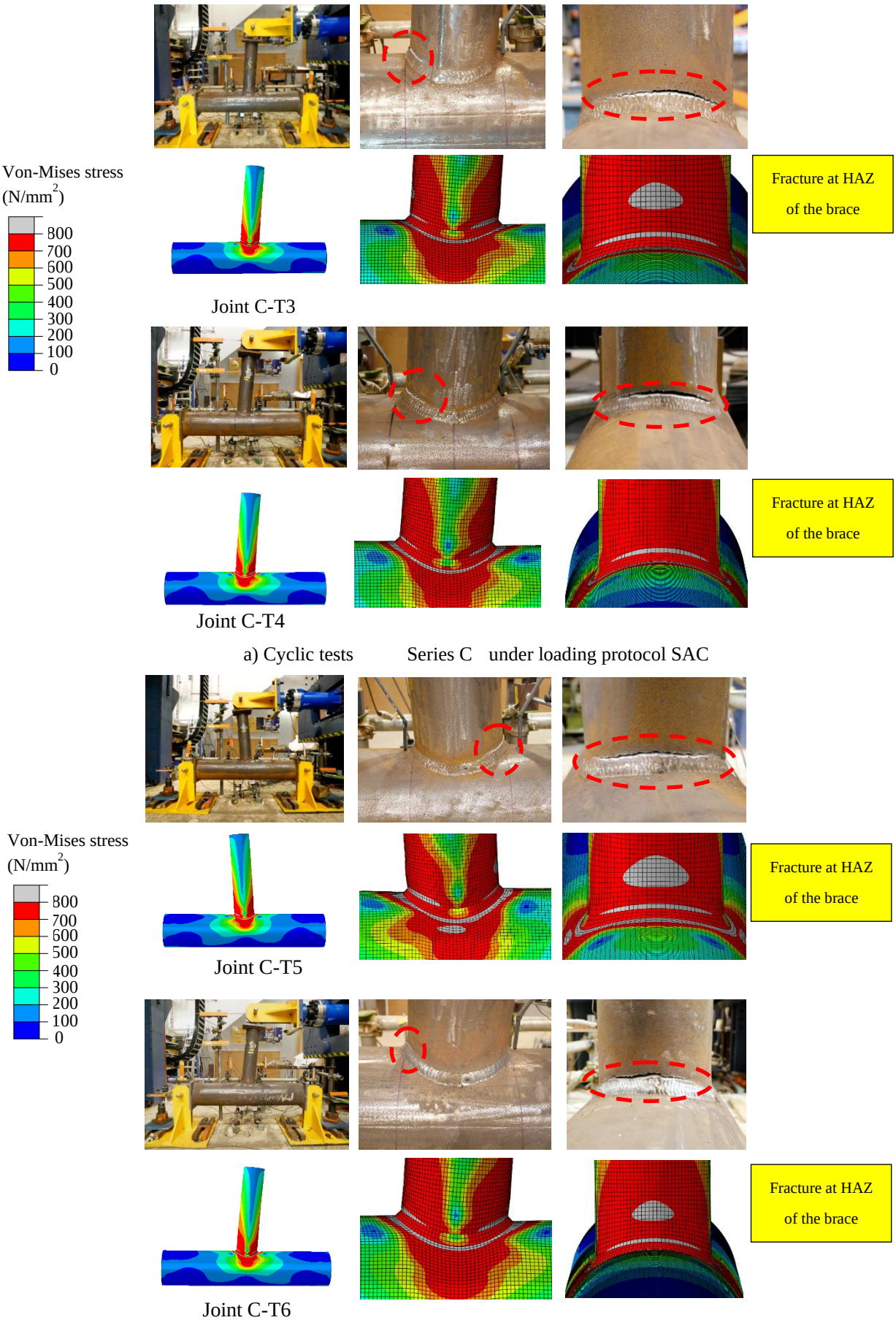

a) Cyclic tests Series C under loading protocol SAC

b) Cyclic tests Series C under loading protocol ECCS

Figure 8 Typical failure modes of T-joints under cyclic actions

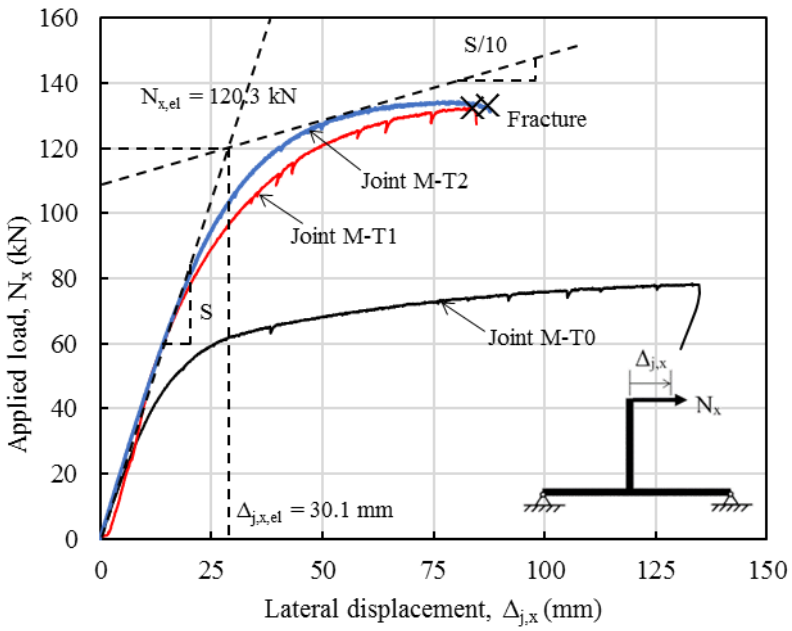

Series M

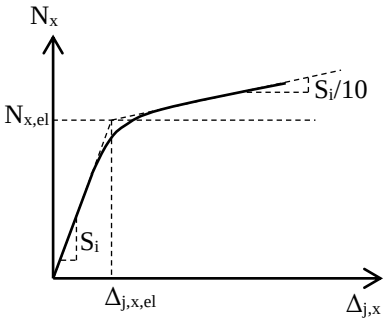

Reference elastic force, $N_{x,el}$ and elastic displacement , $\Delta_{j,x,el}$ to ECCS

Figure 9 Applied load-lateral displacement (N_x – $\Delta_{j,x}$) curves of T-joints under monotonic actions

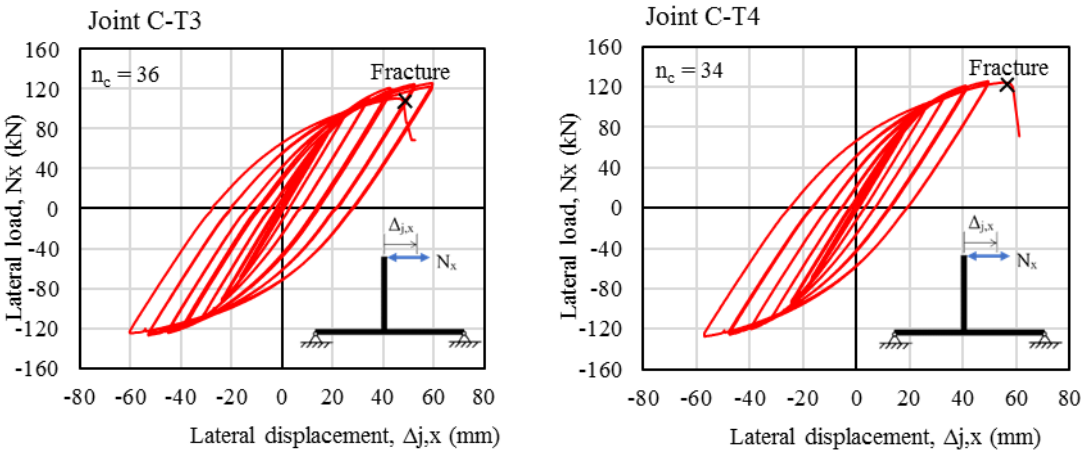

a) Loading Protocol SAC

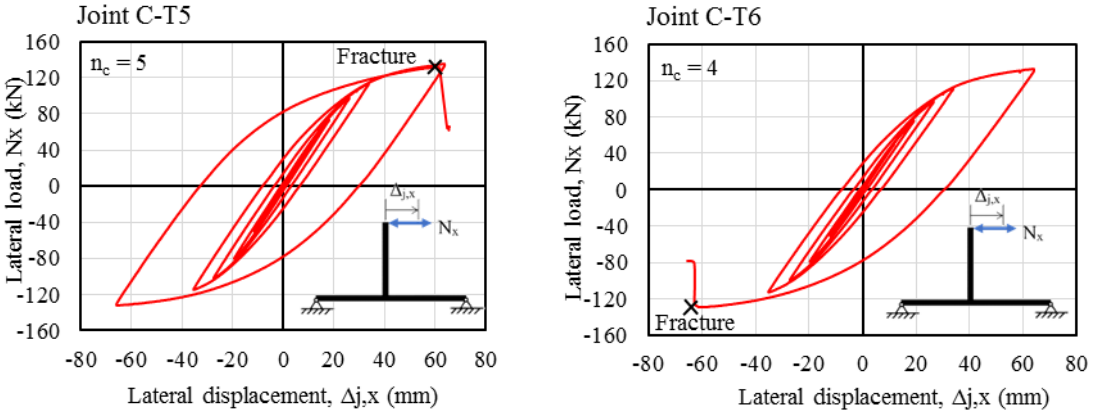

b) Loading Protocol ECCS

Figure 10 Applied load-lateral displacement ($N_x - \Delta_{j,x}$) curves of T-joints under cyclic actions

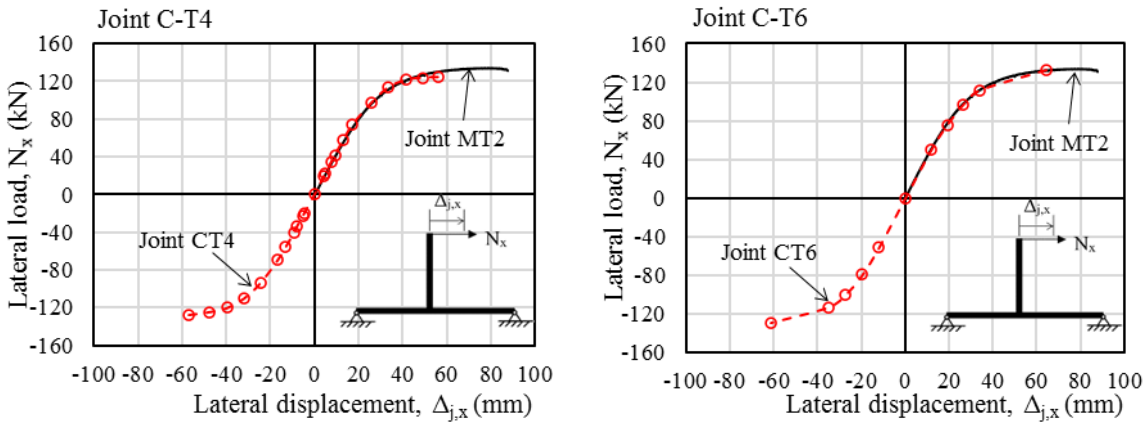

Figure 11 Skeleton curves of T-joints under cyclic actions

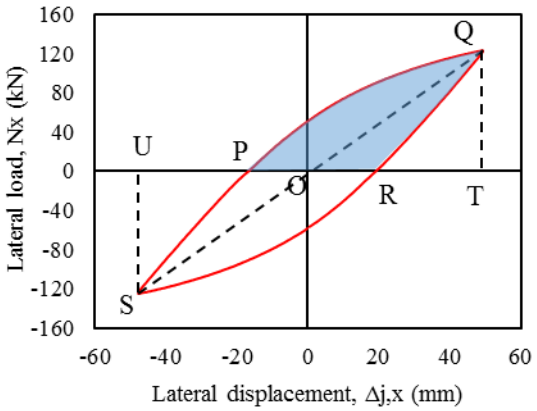

Figure 12 Definition of areas A_{PQR} and A_{RSP}

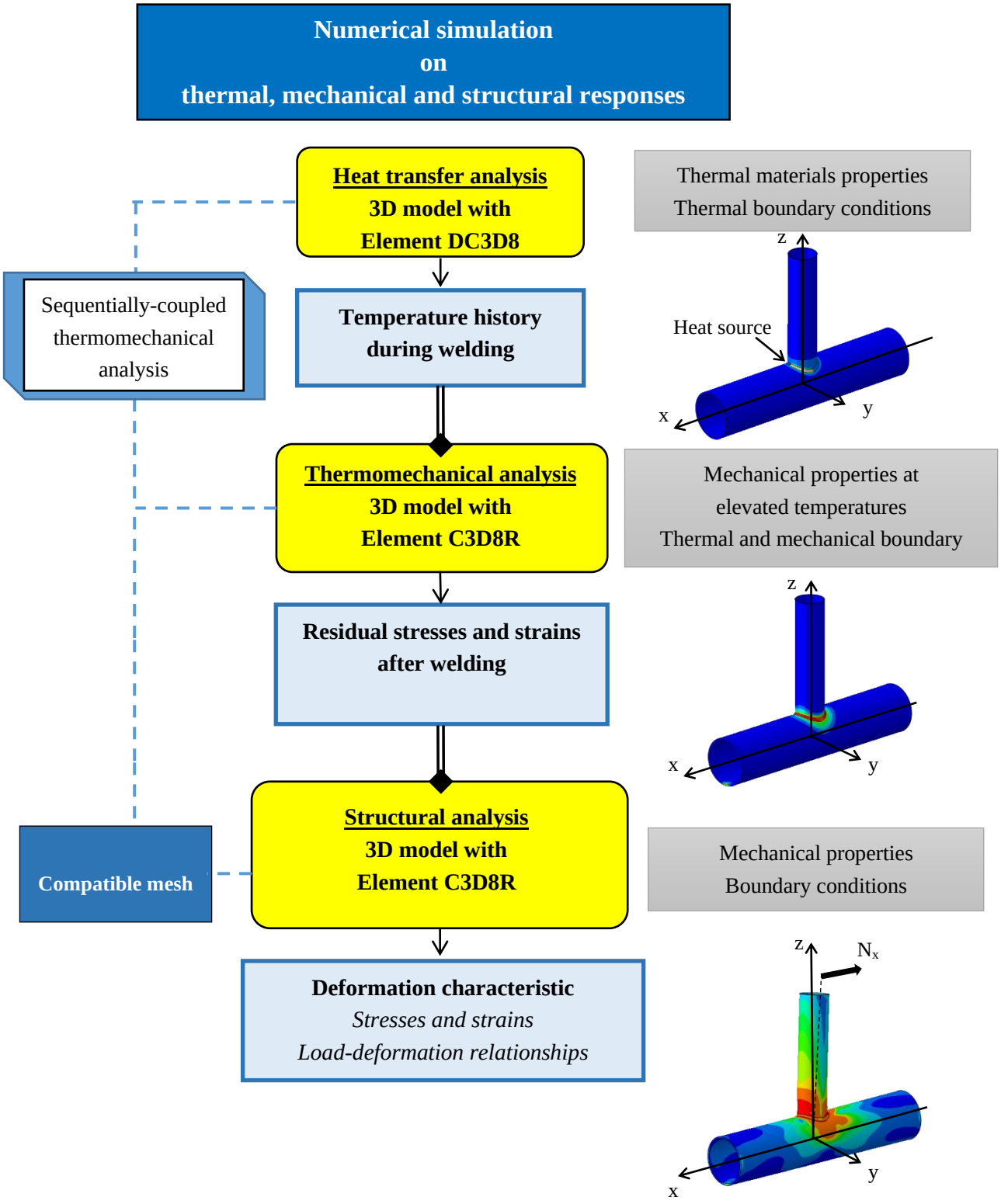

Figure 13 **An overview on integrated numerical modelling approach**

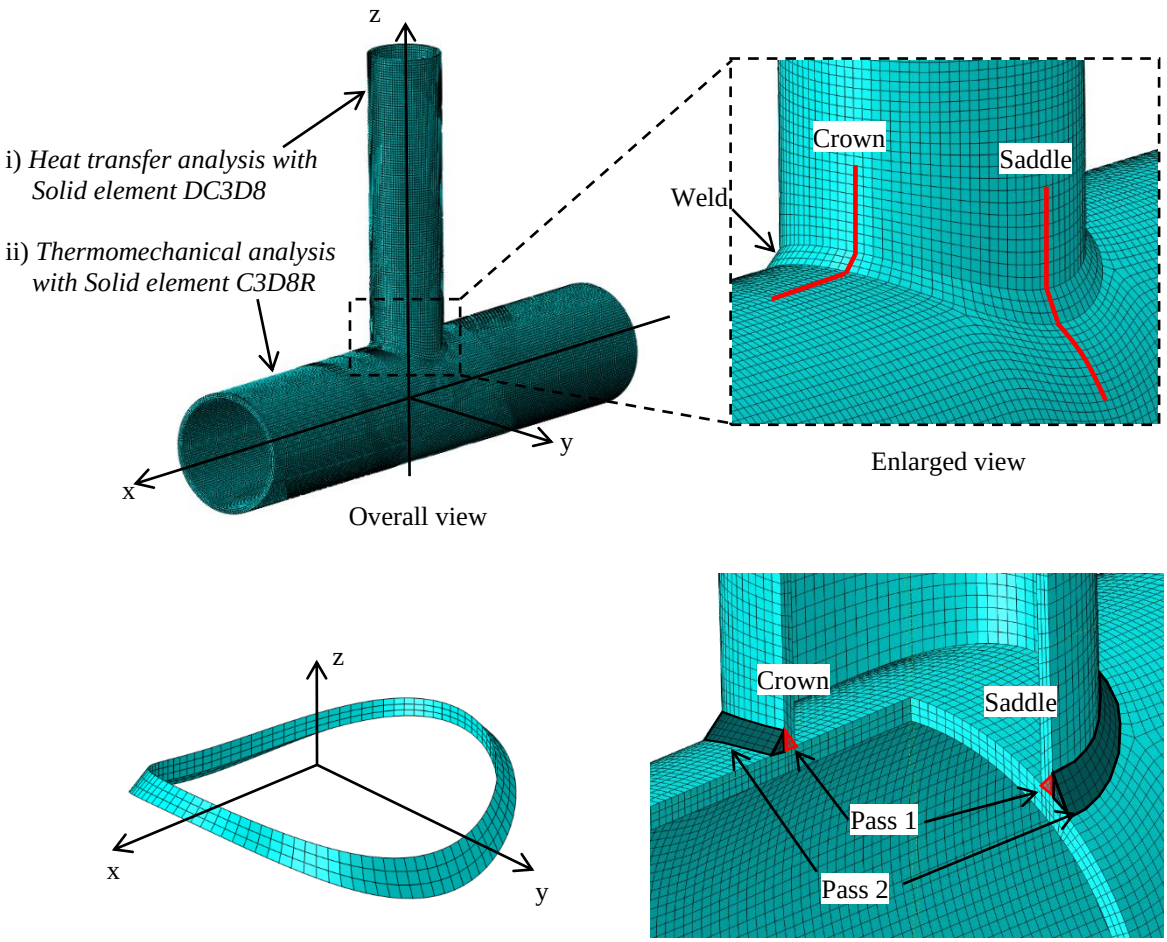

Typical arrangement of solid elements for the weld collar

Typical mesh configuration at the brace/chord junction

Figure 14 Finite element mesh of a typical T-joint

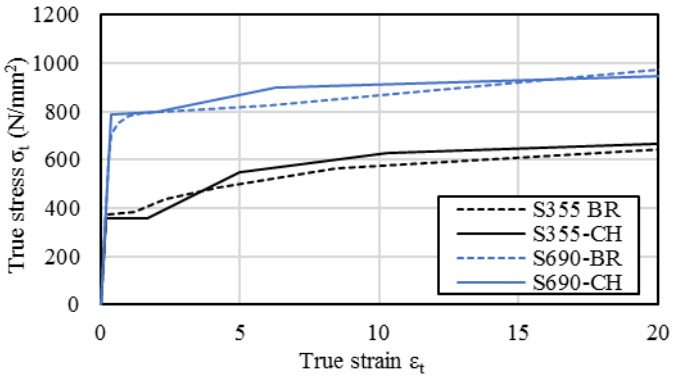

a) True stress-strain curves of S355 and S690 CFCHS

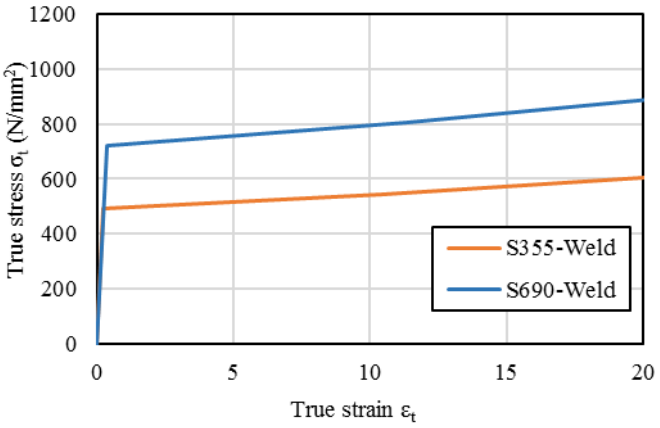

b) True stress-strain curve of weld metal

Figure 15 Stress-strain curves for the proposed models

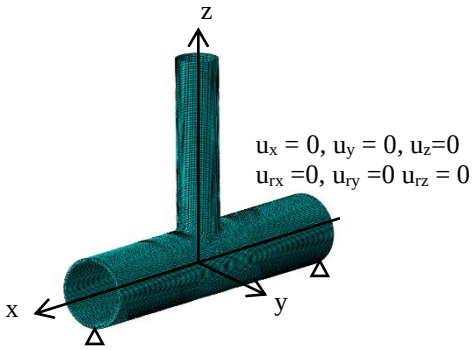

a) For both heat transfer analysis and thermomechanical analysis

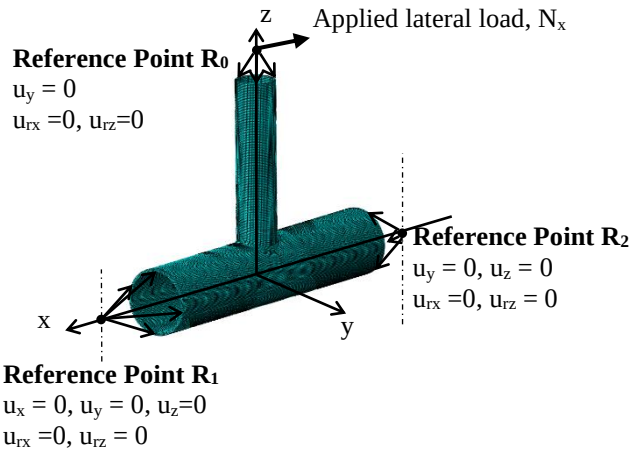

b) For structural analysis

Figure 16 Boundary conditions for the proposed models

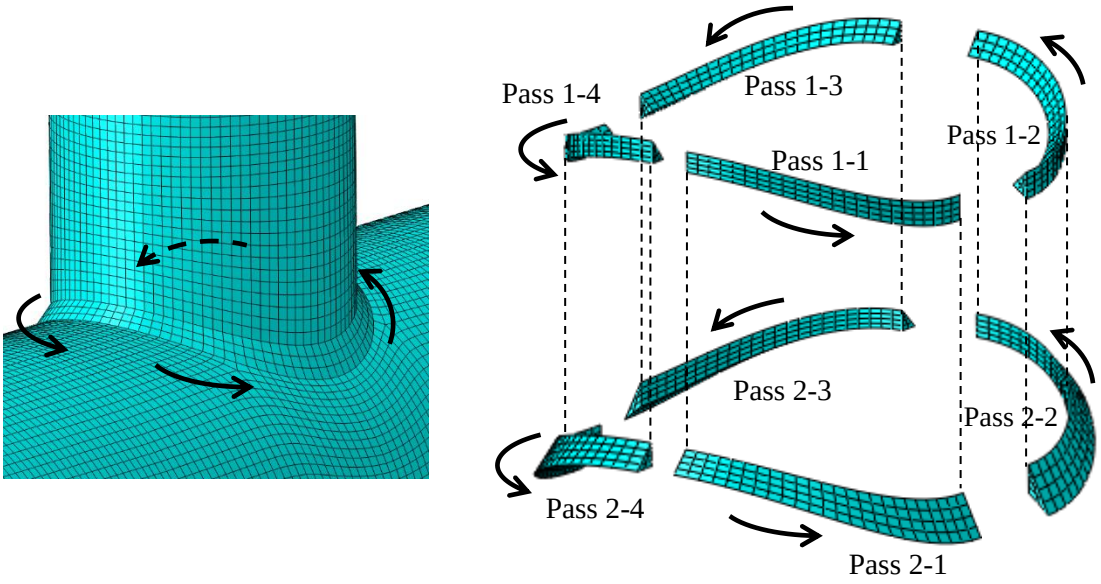

Figure 17 Welding sequences for the brace/chord junction

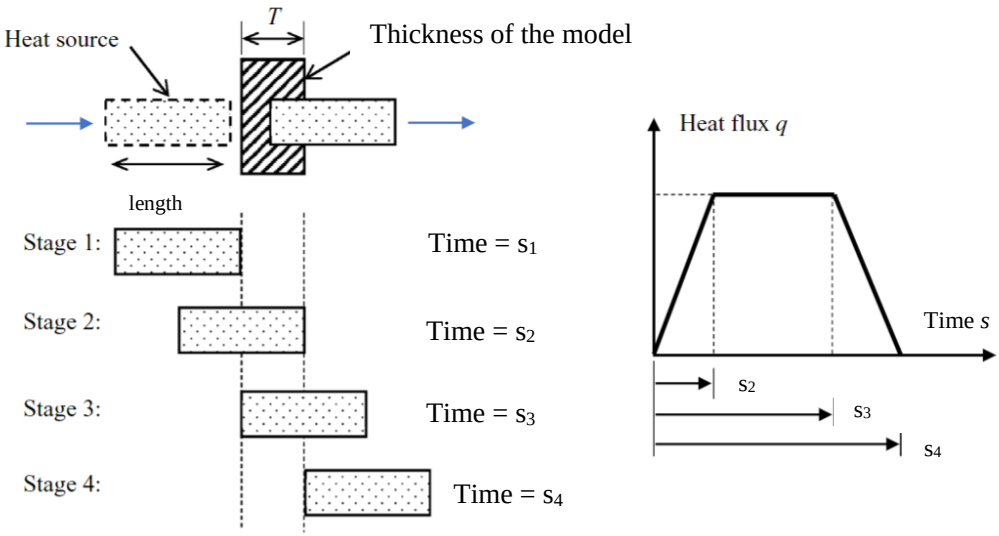

Figure 18 A ramp heat source model

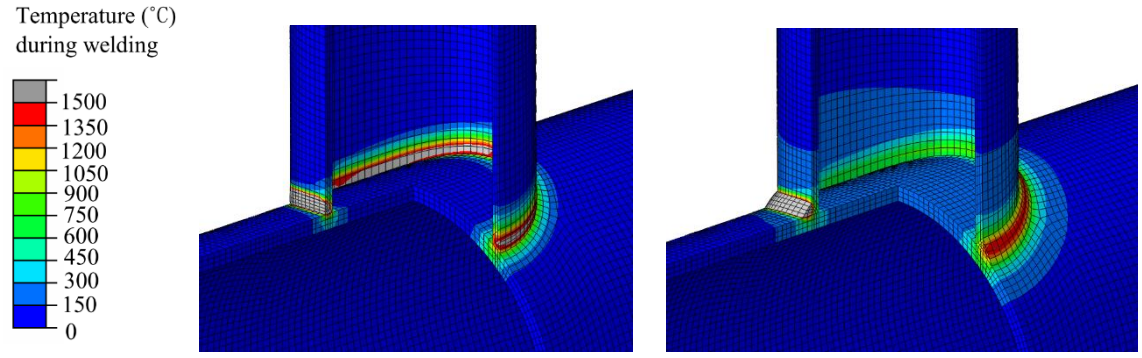

a) Welding Pass 1 b) Welding Pass 2

Figure 19 Transient temperature distributions at the brace/chord junction immediately after welding

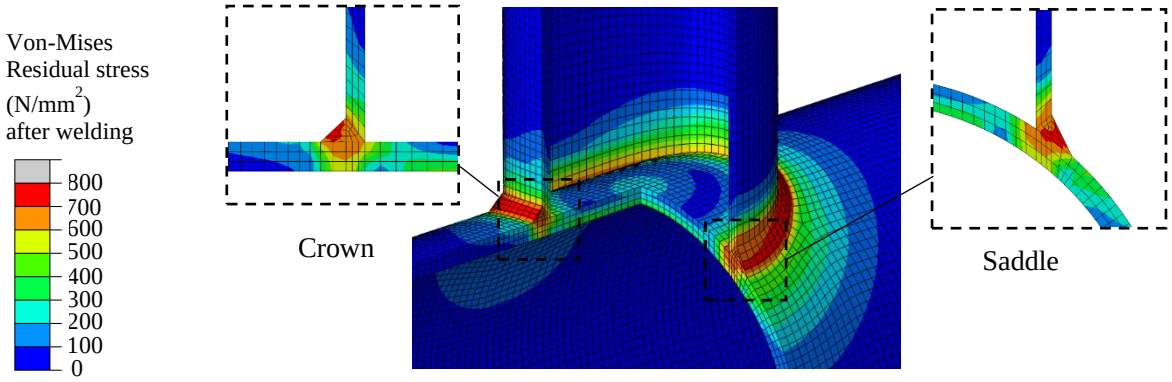

Figure 20 Residual stress distributions at the brace/chord junction after welding

Deformed shape

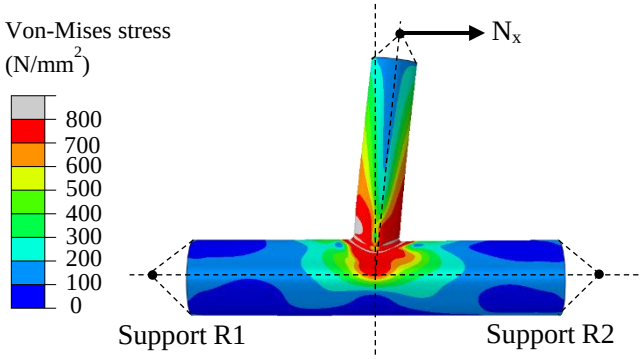

Deformed shape

a) Deformed shapes of Joint M-T2

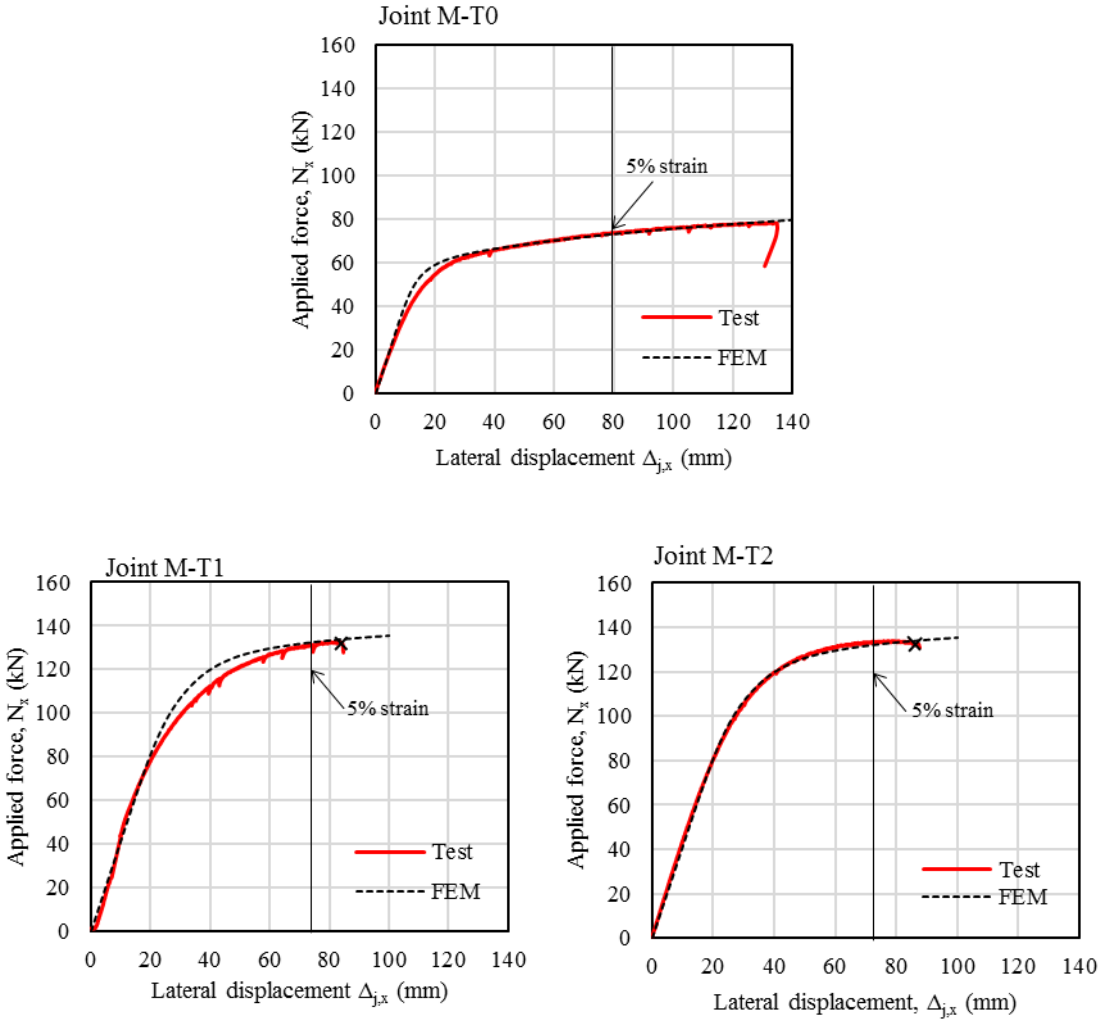

b) Applied load-lateral displacement (N_x – $\Delta_{j,x}$) curves

Figure 21 Comparison of experimental and numerical results for Series M

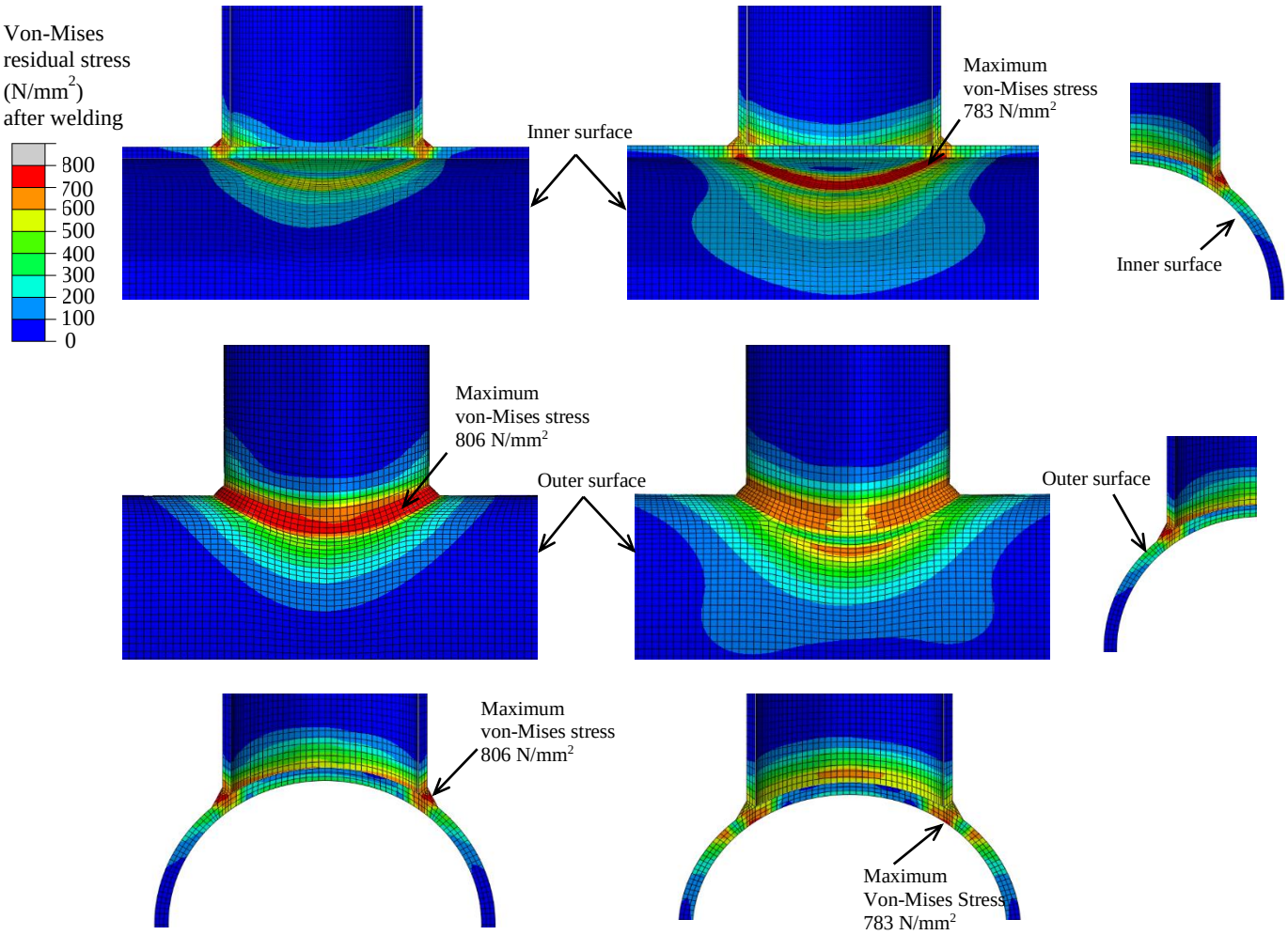

a) q = 1.35 kJ/mm
with two welding passes

b) q = 2.0 kJ/mm
with a single welding pass

Figure 22 Comparison on welding induced residual stresses against heat input energy

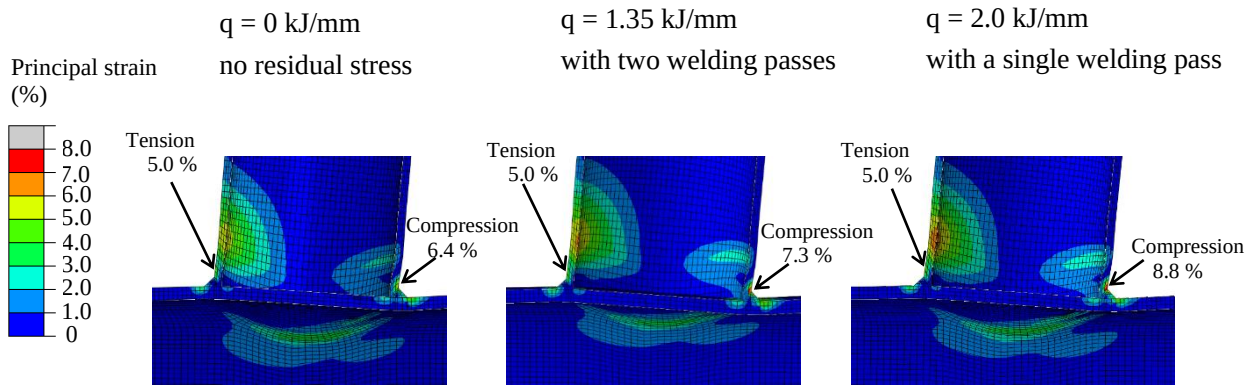

a) Principal strains

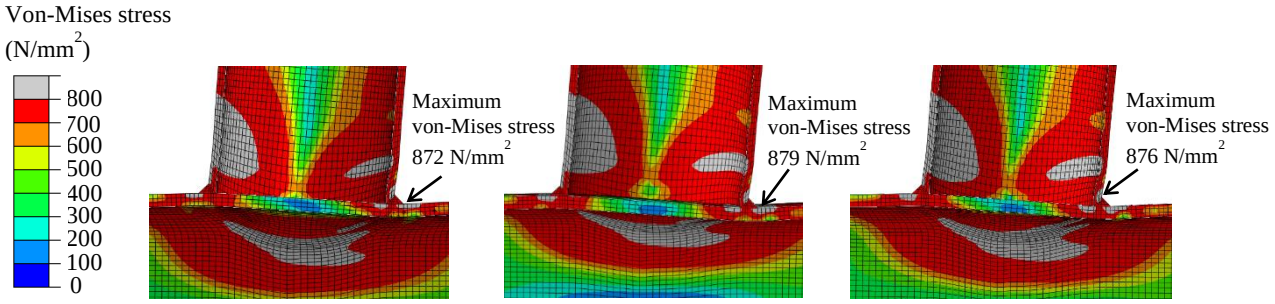

b) Von-Mises stresses

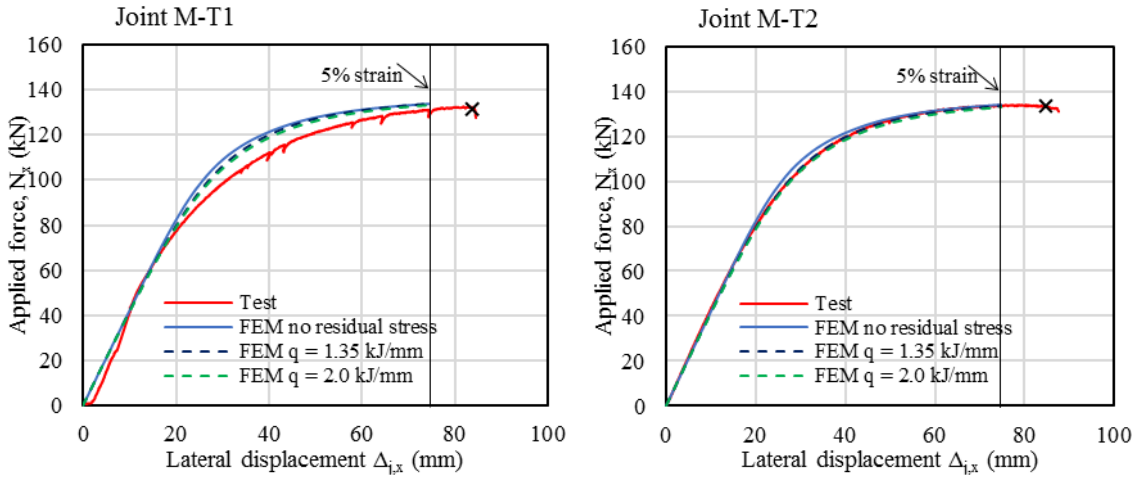

c) Applied load – lateral displacement (N_x – $\Delta_{j,x}$) curves

Figure 23 Comparison on different deformation characteristics of the proposed models

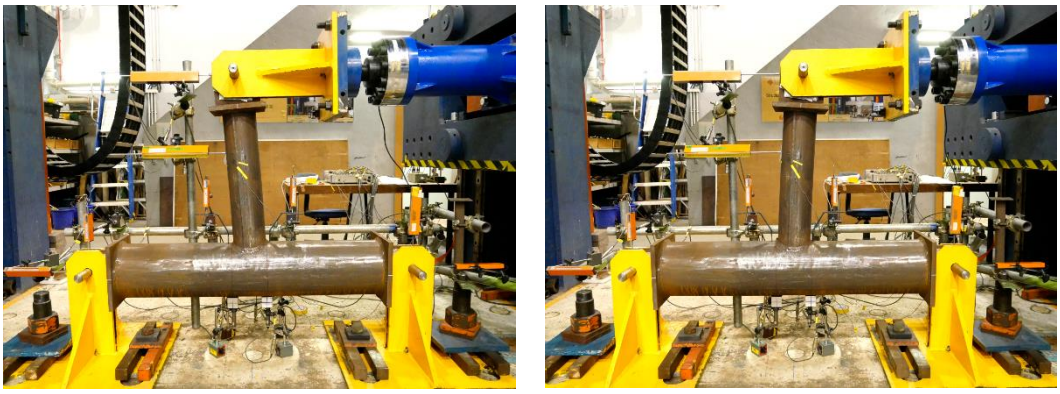

Deformed shape at the 36 th cycle
$\Delta_{j,x}$ = -52.6 mm

Deformed shape at the 36 th cycle
$\Delta_{j,x}$ = 59.5 mm

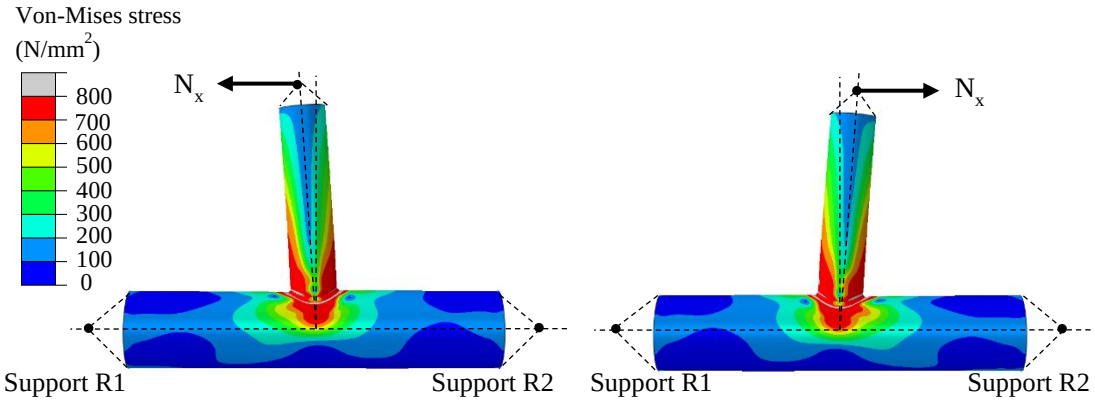

Deformed shape at the 36th cycle
Δ_{jx} = -52.6 mm

Deformed shape at the 36th cycle
Δ_{jx} = 59.5 mm

Joint C-T3

Figure 24 Comparison of experimental and numerical results for Series C

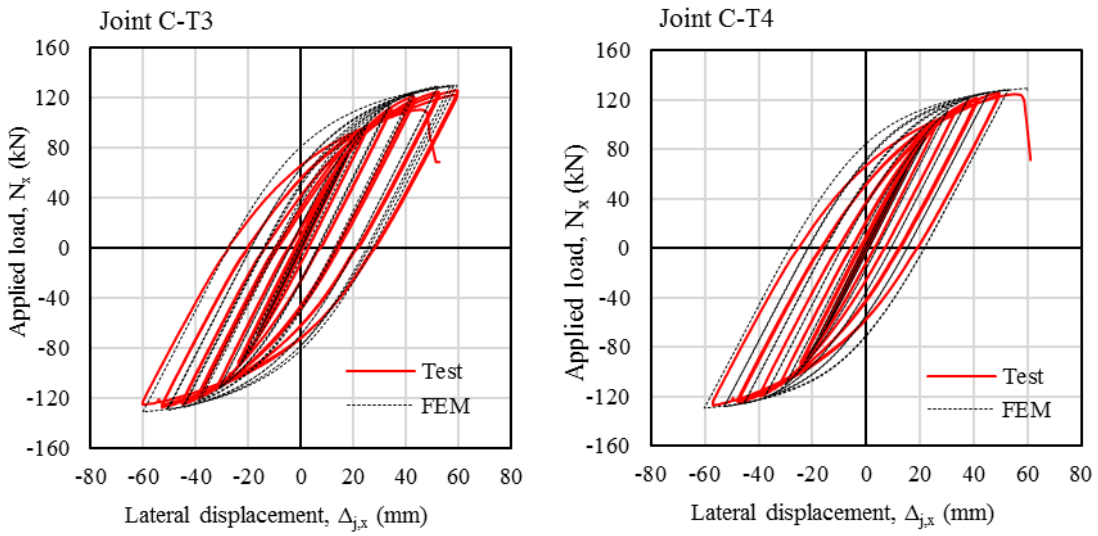

a) Applied load-lateral displacement (N_x – $\Delta_{j,x}$) curves under Loading Protocol SAC

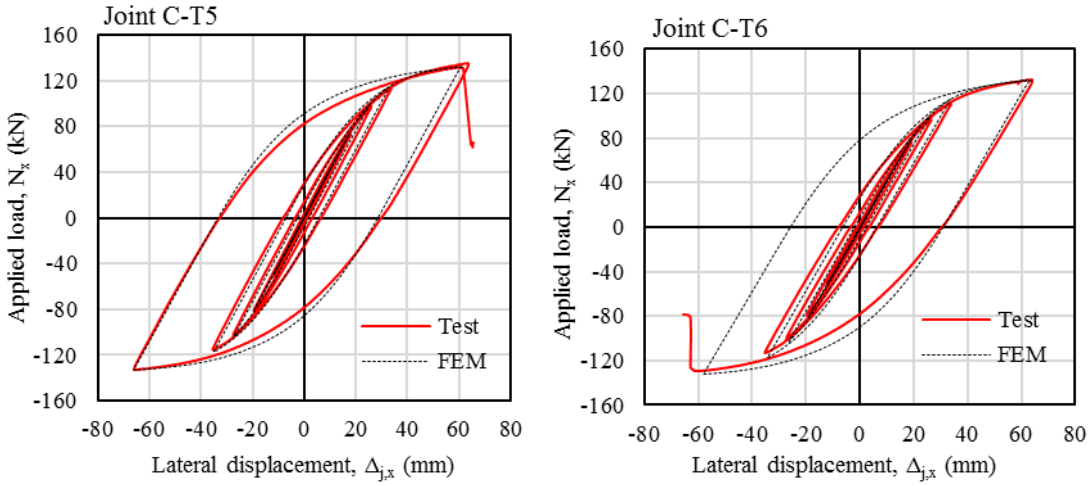

b) Applied load-lateral displacement (N_x – $\Delta_{j,x}$) curves under Loading Protocol ECCS

Figure 25 Comparison of experimental and numerical results for Series C

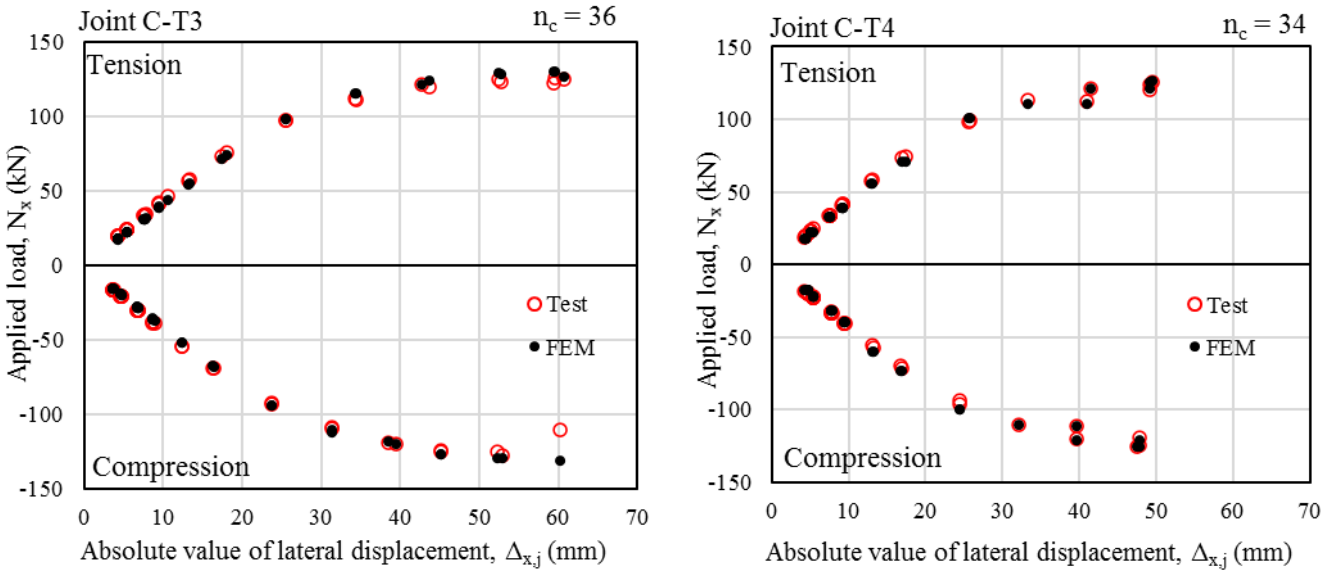

a) $N_{x,max} - \Delta_{j,x}$ curves under Loading Protocol SAC

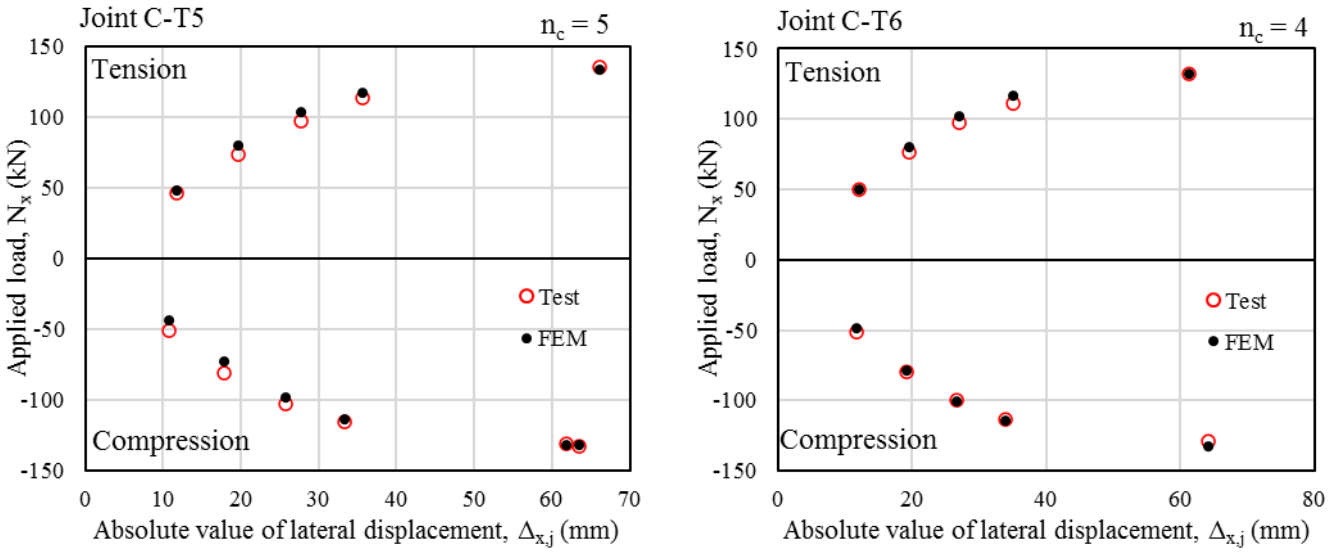

b) $N_{x,max} - \Delta_{j,x}$ curves under Loading Protocol ECCS

Figure 26 Comparison of experimental and numerical results for Series C – Maximum values

Table 1 Test programme for T-joints between S690 CFCHS under brace in-plane bending

Series	Joint	Loading type	Loading protocol	Steel grade	Chord $d_0 \times t_0$ (mm×mm)	*Section class of the chord	Brace $d_1 \times t_1$ (mm×mm)	*Section class of the brace	α	β	γ	τ
M	M-T0	Monotonic	/	S355	250×10	Class 1	150×6	Class 1	9.6	0.6	12.5	0.6
	M-T1			S690	250×10	Class 3	150×6	Class 3	9.6	0.6	12.5	0.6
	M-T2			S690	250×10	Class 3	150×6	Class 3	9.6	0.6	12.5	0.6
C	C-T3	Cyclic	SAC	S690	250×10	Class 3	150×6	Class 3	9.6	0.6	12.5	0.6
	C-T4			S690	250×10	Class 3	150×6	Class 3	9.6	0.6	12.5	0.6
	C-T5		ECCS	S690	250×10	Class 3	150×6	Class 3	9.6	0.6	12.5	0.6
	C-T6			S690	250×10	Class 3	150×6	Class 3	9.6	0.6	12.5	0.6

Table 2 Measured geometric dimensions of T-joints

Joint	Chord			Brace		
	Length L_0 (mm)	Diameter d_0 (mm)	Wall thickness, t_0 (mm)	Length L_1 (mm)	Diameter d_1 (mm)	Wall thickness, t_1 (mm)
M-T0	1199.3	251.6	9.9	599.3	151.4	5.9
M-T1	1197.9	251.8	10.0	599.2	152.6	5.9
M-T2	1199.3	251.9	9.9	599.3	152.2	6.0
C-T3	1198.8	251.9	9.9	599.3	152.2	5.8
C-T4	1200.7	251.1	9.8	599.6	152.5	5.9
C-T5	1202.5	252.1	9.9	599.0	152.0	6.0
C-T6	1199.0	251.8	10.0	599.3	151.5	5.9

Table 3 Chemical compositions (%) of welding electrodes

Electrode	C	**Si**	**Mn**	P	S	Cr	Ni	Mo	Cu
ER110S-G	0.090	0.80	1.70	0.015	0.015	0.3	1.85	0.6	0.1
E71T-1	0.055	0.38	1.35	0.015	0.010	-	-	-	-

Table 4 Nominal mechanical properties of welding electrodes

Standard	Electrode	Steel grade	Supplier	Weld method	Diameter (mm)	Yield strength (N/mm^2)	Tensile strength (N/mm^2)	Elongation (%)
AWS A5.28	ER110S-G	S690	Bohler	GMAW	1.2	720	880	15
AWS A5.20	E71T-1	S355	Lanyu	GMAW	1.2	490	580	27

Table 5 Summary of results of standard tensile tests

Steel	Plate thickness (mm)	Young's modulus E (kN/mm^2)	Yield strength f_y (N/mm^2)	Tensile strength f_u (N/mm^2)	f_u / f_y
S355-BR	6	207	371	536	1.44
S355-CH	10	205	365	590	1.62
S690-BR	6	202	747	811	1.08
S690-CH	10	201	766	828	1.08

Table 6 Summary of test results of T-joints between CFCHS under monotonic brace in-plane bending

Joint	Steel grade	Test results				EN 1993-1-8		Finite element results		
		Failure mode	Load	Displacement at failure	Moment resistances	Design resistances		Displacement at failure	Moment resistances	
			$N_{x,Rt}$ (kN)	$\Delta_{j,x,f}$ (mm)	$M_{j,Rt}$ (kNm)	$M_{j,Rd}$ (kNm)	$\frac{M_{j,Rt}}{M_{j,Rd}}$	$\Delta_{j,x,FE}$ (mm)	$M_{j,FE}$ (kNm)	$\frac{M_{j,Rt}}{M_{j,FE}}$
M-T0	S355	B-pb	76.4	> 135.0	58.1	46.2	1.26	78.3	56.7	1.02
M-T1	S690	BF	132.7	84.7	100.9	79.6	1.27	72.2	101.5	0.99
M-T2	S690	BF	134.2	87.7	102.0		1.28	73.2	101.5	1.00

Notes:

B-pb denotes a plastic local buckling in the brace;

BF denotes a fracture in the brace in the vicinity of the welded brace/chord junctions.

Table 7 Summary of test results of T-joints under cyclic brace in-plane bending

Joint	Loading protocol	Test results								Finite element results					
		Failure mode	$N_{x,Rt+}$ (kN)	$\Delta_{j,x,Rt+}$ (mm)	$M_{j,Rt+}$ (kNm)	$N_{x,Rt-}$ (kN)	$\Delta_{j,x,Rt-}$ (mm)	$M_{j,Rt-}$ (kNm)	$\theta_{b,m}$ (rad)	n_c	$N_{x,FE+}$ (kN)	$M_{j,FE+}$ (kNm)	$\frac{M_{j,Rt+}}{M_{j,FE+}}$	$N_{x,FE-}$ (kN)	$M_{j,FE-}$ (kNm)	$\frac{M_{j,Rt-}}{M_{j,FE-}}$
C-T3	SAC	BF	125.9	59.5	95.7	-127.1	-52.6	-96.6	0.080	36	130.1	98.9	0.97	-128.9	-99.3	0.97
C-T4	SAC	BF	125.7	49.3	95.5	-127.3	-47.7	-96.7	0.065	34	125.9	98.2	0.97	-125.7	-98.2	0.98
C-T5	ECCS	BF	134.9	63.4	102.5	-132.8	-66.1	-100.9	0.087	5	133.0	100.2	1.02	-131.9	-101.0	1.00
C-T6	ECCS	BF	132.4	64.2	100.6	-129.2	-61.4	-98.2	0.084	4	131.8	100.6	1.00	-132.4	-100.2	0.98

Notes:

BF denotes a fracture in the brace in the vicinity of the welded brace/chord junctions;

$N_{x,Rt+}$ and $N_{x,Rt-}$ denote measured maximum positive and negative loads, respectively;

$\Delta_{j,x,Rt+}$ and $\Delta_{j,x,Rt-}$ denote measured maximum positive and negative displacements, respectively;

$M_{j,Rt+}$ and $M_{j,Rt-}$ denote measured maximum positive and negative moments, respectively;

$\theta_{b,m}$ denotes measured maximum interstorey drift;

n_c denotes number of cycles completed before failure;

$N_{x,FE+}$ and $N_{x,FE-}$ denote predicted maximum positive and negative loads, respectively; and

$M_{j,FE+}$ and $M_{j,FE-}$ denote predicted maximum positive and negative moments, respectively.

Table 8 Energy dissipation parameters of T-joints under cyclic actions

a) Loading Protocol SAC

	Dissipated Energy, E_i (kNm)	
	Joint C-T3	
Cycle	**Test**	**FEM**
19	0.013	0.0001
20	0.013	0.0001
21	0.013	0.0001
22	0.013	0.0001
23	0.040	0.002
24	0.037	0.019
25	0.133	0.022
26	0.124	0.330
27	0.644	0.416
28	1.742	1.528
29	1.909	1.913
30	3.685	3.906
31	4.031	4.376
32	6.060	6.560
33	6.562	7.069
34	8.722	8.881
35	9.131	9.462
36	11.396	11.658
Accumulative energy dissipation E_{acc} (kNm)	54.27	56.14
E_{el} (kNm)	1.80	1.80
Energy dissipation ratio, η_a	30.15	31.19

	Dissipated Energy, E_i (kNm)	
	Joint C-T4	
Cycle	**Test**	**FEM**
19	0.016	0.0001
20	0.016	0.0001
21	0.016	0.0001
22	0.016	0.0001
23	0.052	0.002
24	0.047	0.001
25	0.157	0.013
26	0.129	0.140
27	0.730	0.212
28	0.726	0.213
29	1.943	1.116
30	2.060	1.327
31	3.931	3.019
32	4.140	3.492
33	6.564	5.696
34	6.746	6.193
-	-	-
-	-	-
Accumulative energy dissipation E_{acc} (kNm)	27.29	21.42
E_{el} (kNm)	1.80	1.80
Energy dissipation ratio, η_a	15.16	11.90

b) Loading Protocol ECCS

	Dissipated Energy, E_i ((kNm)	
	Joint C-T5	
Cycle	**Test**	**FEM**
1	0.0359	0.0020
2	0.0224	0.0424
3	0.9172	0.5508
4	2.3343	1.9856
5	12.3746	12.2814
Accumulative energy dissipation E_{acc} (kNm)	15.89	15.33
E_{el} (kNm)	1.80	1.80
Energy dissipation ratio, η_a	8.83	8.51

	Dissipated Energy, E_i (kNm)	
	Joint C-T6	
Cycle	**Test**	**FEM**
1	0.3811	0.0004
2	0.2739	0.0614
3	0.9360	0.5635
4	2.3002	1.9808
-	-	-
Accumulative energy dissipation E_{acc} (kNm)	3.55	2.61
E_{el} (kNm)	1.80	1.80
Energy dissipation ratio, η_a	1.97	1.45

Table 9 Comparison on effects of residual stresses onto joint resistances

Joint	Steel grade	Test results	Numerical predictions					
			q = 0.0 kJ/mm		q = 1.35 kJ/mm		q = 2.0 kJ/mm	
		$M_{j,Rt}$ (kNm)	$M_{j,FE}$ (kNm)	$\frac{M_{j,Rt}}{M_{j,FE}}$	$M_{j,FE}$ (kNm)	$\frac{M_{j,Rt}}{M_{j,FE}}$	$M_{j,FE}$ (kNm)	$\frac{M_{j,Rt}}{M_{j,FE}}$
M-T0	S355	58.1	56.7	1.02	56.7	1.02	56.9	1.02
M-T1	S690	100.9	102.1	0.99	101.5	1.00	101.1	1.00
M-T2	S690	102.0	101.9	1.00	101.5	1.01	101.1	1.01

Table 10 Comparison of measured and predicted lateral displacements of the joints under cyclic actions

a) Joint C-T3

Cycle	Maximum measured displacement (mm)	Load		Discrepancy ratio (%)	Maximum measured displacement (mm)	Load		Discrepancy ratio (%)
		$N_{x,Rt}$ (kN)	$N_{x,FE}$ (kN)			$N_{x,Rt}$ (kN)	$N_{x,FE}$ (kN)	
19 to 22	-8.72	-38.27	-36.04	1.73	9.75	42.91	40.32	2.00
23 to 24	-12.45	-53.89	-51.47	1.88	13.26	57.34	54.76	1.98
25 to 26	-16.36	-68.94	-67.36	1.23	17.81	74.57	73.00	1.21
27 to 28	-23.74	-92.50	-93.42	0.72	25.55	97.44	98.19	0.58
29 to 30	-31.31	-108.93	-111.17	1.74	34.32	112.03	115.40	2.59
31 to 32	-38.98	-119.27	-119.06	0.17	43.17	120.53	123.12	1.99
33 to 34	-45.13	-124.09	-126.59	1.94	52.56	124.09	128.76	3.59
35 to 36	-52.59	-125.93	-128.87	2.28	59.53	124.21	130.06	4.50
			Average	**1.46**			**Average**	**2.30**

Note:

Discrepancy ratio = $\frac{|N_{x,Rt} - N_{x,FE}|}{|N_{x,FE,max}|}$

b) Joint C-T4

Cycle	Maximum measured displacement (mm)	Load		Discrepancy ratio (%)	Maximum measured displacement (mm)	Load		Discrepancy ratio (%)
		$N_{x,Rt}$ (kN)	$N_{x,FE}$ (kN)			$N_{x,Rt}$ (kN)	$N_{x,FE}$ (kN)	
19 to 22	-9.46	-40.28	-39.60	0.54	9.20	41.65	38.62	2.40
23 to 24	-13.18	-56.19	-60.17	3.17	13.01	57.80	55.99	1.43
25 to 26	-16.77	-70.44	-73.06	2.09	17.16	73.77	71.20	2.04
27 to 28	-24.44	-94.57	-100.35	4.60	25.65	98.70	101.50	2.23
29 to 30	-35.83	-110.53	-110.85	0.25	37.14	112.72	110.92	1.43
31 to 32	-43.74	-119.73	-120.94	0.96	45.36	120.99	121.26	0.21
33 to 34	-47.68	-124.90	-125.76	0.69	49.34	124.67	125.79	0.89
			Average	**1.76**			**Average**	**1.52**

c) Joint C-T5

Cycle	Maximum measured displacement (mm)	Load		Discrepancy ratio (%)	Maximum measured displacement (mm)	Load		Discrepancy ratio (%)
		$N_{x,Rt}$ (kN)	$N_{x,FE}$ (kN)			$N_{x,Rt}$ (kN)	$N_{x,FE}$ (kN)	
1	10.70	-51.02	-44.25	5.14	-11.70	45.96	48.38	-1.82
2	17.82	-81.12	-73.03	6.15	-19.63	73.31	79.79	-4.87
3	25.78	-102.95	-98.77	3.18	-27.69	97.44	103.52	-4.57
4	33.42	-115.36	-113.83	1.16	-35.68	113.29	117.34	-3.05
5	63.43	-132.82	-131.87	0.72	-66.09	134.89	132.95	1.46
6	61.78	-131.45	-131.64	-0.14	-	-	-	-
			Average	**2.75**			**Average**	**3.15**

d) Joint C-T6

Cycle	Maximum measured displacement (mm)	Load		Discrepancy ratio (%)	Maximum measured displacement (mm)	Load		Discrepancy ratio (%)
		$N_{x,Rt}$ (kN)	$N_{x,FE}$ (kN)			$N_{x,Rt}$ (kN)	$N_{x,FE}$ (kN)	
1	11.81	-51.25	-48.83	1.83	-12.02	49.87	49.70	0.13
2	19.22	-79.51	-78.27	0.94	-19.61	76.06	79.74	-2.78
3	26.62	-99.73	-100.84	-0.84	-27.03	97.21	102.09	-3.69
4	33.97	-113.06	-114.53	-1.11	-35.15	111.45	116.83	-4.06
5	64.17	-129.15	-132.37	-2.43	-61.36	132.36	131.82	0.41
			Average	**1.43**			**Average**	**2.21**